CHARACTERIZATIONS OF ZINC AMMONIUM PHOSPHATE, $ZnNH_4PO_4$ [ZAP] SINGLE CRYSTAL

PhD DISSERTATION

PHYO MAW TUN THAN

DEPARTMENT OF PHYSICS
UNIVERSITY OF YANGON
MYANMAR

MARCH 2008

CHARACTERIZATIONS OF ZINC AMMONIUM PHOSPHATE, $ZnNH_4PO_4$ [ZAP] SINGLE CRYSTAL

PHYO MAW TUN THAN

THIS DISSERTATION IS SUBMITTED TO THE BOARD OF EXAMINERS IN PHYSICS, NIVERSITY OF YANGON FOR THE DEGREE OF DOCTOR OF PHILOSOPHY

EXTERNAL EXAMINER **CHAIRPERSON** **EXTERNAL EXAMINER**

REFEREE **SUPERVISOR**

CONTENTS

ACKNOWLEDGEMENTS

I would like to thank Professor Dr Win Win Thar, PhD(*YU*), Professor and Head of Department of Physics, University of Yangon for her kind permission to carry out this work.

I also wish to express my thanks to Professor Dr Pho Kaung, DSc(*Hokkaido*), Head of Universities' Research Centre (URC) and Director of Asia Research Centre (ARC) for his permission to use the laboratory facilities.

I am greatly indebted to my Supervisor Dr Win Kyaw, PhD(*YU*), Assistant Lecturer, Department of Physics, University of Yangon, for his valuable guidance.

I am also grateful to my parents for their support and encouragement without which this dissertation will not be possible.

ABSTRACT

Single crystals of $ZnNH_4PO_4$ [ZAP] have been grown by slow evaporation of aqueous solutions containing the equimolar ratio of the laboratory grade of Zinc Sulphate, $ZnSO_4$ and Ammonium Dihydrogen Phosphate, $NH_4H_2PO_4$ [ADP] and distilled-water. Structural, vibrational and thermal investigations of those crystals were characterized by XRD, Raman scattering, FTIR spectroscopic methods and TG-DTA measurements. Temperature dependent electrical conductivity and dielectric measurement of ZAP crystal was carried out to study the decomposition process at high temperature.

LIST OF FIGURES

LIST OF TABLES

CHAPTER I
INTRODUCTION

In general, the value of a crystal property depends on the direction of measurement, the crystal is described as anisotropic with respect to that property. There are exceptions; for example, crystals having cubic symmetry are optically isotropic although they are anisotropic with respect to elasticity. For this reasons, a description of the physical behaviour of a material has to be based on knowledge of crystal structure. Ionic conduction of a material depends on the presence of vacant sites into which ions can move. In the absence of a field, thermal vibrations proportional to kT cause ions and vacancies to exchange sites [2, 7, 21].

Picturing the structures of crystals _ their orderliness and symmetry, and the atoms are bonded in them with fixed position. The orderly sites pictured in the structural diagrams are only the average positions of the atoms, the positions about which they vibrate. Thus, the orderliness of a crystal is at best an average orderliness. At any instant the crystal always has some disorder, since the unorganized vibrations of the atoms displace them from their orderly sites in a random way. In most crystals each atom constantly return to its own site as it vibrates; the atoms do not interchange sites or stray permanently from their proper places [12, 13, 17, 18].

Heating a crystal increases the vigor of atomic vibrations until the atoms hit one another hard enough to make spaces in which they can move past one another. Then, the crystal melts. At a higher temperature, the molecules vibrate more rapidly and move further away from each other (i.e. slight increase in volume of the solids). Very strong forces hold the molecules together, allowing them to move only slightly apart from each other. Then we can see only very small expansions in solids. Hence, the most solids expand but its expansion is the least compared with liquids and gases. When heated a solid, mass of given solid is unchanged while volume is increase (least expansion) and density is decreased [18, 20].

Generally speaking, the phenomena associated with hydrogen bonding are quite diverse, and attract the physicists to take part in the cooperate research on hydrogen

bonding. In many molecules, where hydrogen takes part in the covalent bonding, the centers of the positive and negative charges do not coincide. Hydrogen bonds are evidently directional. Such a type of those bondings is known as secondary bonding. Hydrogen bond has a wide distribution in the natural materials not only in crystalline substances but also in many organic materials.

$NH_4H_2PO_4$ [ADP] is one of the typical hydrogen-bonded material in which due to the "order-disorder" dynamics of PO_4 dipoles. The crystal structure of (ADP) at room temperature is tetragonal system that consisting of (NH_4^+) and $(H_2PO_4)^-$ ions belonging to the space group D_{2d}^{12}. The unit cell possesses four formula units, that is, Z = 4. According to the international table of crystallography, "D_{2d}" refer that the 2-fold vertical rotational axis contains a 4-fold rotoreflection axis, 2-horizontal rotation axes are situated at bisecting angles between 2-vertical reflection planes.

Crystal of Zinc Sulphate, $ZnSO_4$ belongs to orthorhombic system with the space of *Pmcn*. The unit cell possesses four formula units, that is, Z = 4. The purpose of the present work is carried out on Zinc Ammonium Phosphate, $ZnNH_4PO_4$ [ZAP] from the growth conditions of $ZnSO_4$ and ADP with the vibrational and temperature dependent electrical parameters point of views.

CHAPTER II

STRUCTURAL ANALYSIS AND X-RAY DIFFRACTION

Materials in the crystalline state are common place and they play an important part in everyday life. The household chemical salt, sugar and washing soda, the industrial materials, corundum and germanium, and the precious stones and emeralds, are all examples of such materials. Many crystals are very regular in shape and clearly exhibit a great deal of symmetry. One of the most noticeable features of many crystals, as we have already seen, it is a certain regularity of arrangement of the faces, and we proceed to study the nature of this regularity in greater detail. If we examine a number of drawings of typical crystals or, batten still, a number of crystal models, it is at once apparent that there is a strong tendency for face to be so arranged that the edges formed by a number of them are parallel. This feature is very evident, such a set of faces constitutes a zone, which we can define as a set of faces whose mutual interactions are all parallel. The common direction of edge is that of the zone axis of that particular zone [6, 7, 17, 18].

2.1 X-ray Diffraction

X-ray diffraction is the most widely used and least ambiguous method for the precise determination of the positions of atoms in molecules and solids. Spectroscopic information (NMR, IR and mass spectrometry), does not give such a complete picture for inorganic materials, owing to much greater structural diversity in terms of coordination numbers and geometries. Particularly in inorganic chemistry, the distances derived from the structure give additional information on bonding within and between molecules. For example, particular bond lengths and angles are indicative of certain oxidation states.

2.2 Principles of X-ray Diffraction

X-rays interact with electrons in matter. When a beam of X-rays impinges on a material it is scattered in various directions by the electron clouds of the atoms. If the wavelength of the X-rays is comparable to the separation between the atoms, then interference can occur. For an ordered array of scattering centers (such as atoms or ions in a crystalline solid), this can give rise to interference maxima and

minima. The wavelengths of X-rays used in X-ray diffraction experiments therefore typically lie between 0.6 Å and 1.9 Å.

2.2.1 Generation of X-rays

A beam of electrons striking a metal target will eject electrons (core electrons) from the energy levels close to the nucleus of some of the metal atoms (providing the beam is higher in energy than the energy needed to remove such electrons). Once vacancies have been created, electrons from higher energy levels fall down (decay) into these orbits. The difference in energy between these higher and lower energy levels is then emitted as an X-ray of precise energy ($\Delta E = h\nu$, where ΔE is the energy difference, ν is the frequency of the emitted radiation and h is Planck's constant).

2.2.2 The X-ray Tube

A schematic diagram of a typical X-ray tube is shown in Fig 2.1. The electrons are created by heating a tungsten filament in a vacuum (thermionic emission) and then accelerated by a high voltage (typically 30,000 V) towards a metal target. Core electrons are knocked out of the metal target and the X-rays, characteristic of the metal target, are produced by decay. By making a beryllium window in the tube, because beryllium has a low atomic number and is transparent to X-rays, the X-ray beam escapes from the tube.

A spectrum of the output from an X-ray tube is shown in Fig 2.2. The background is known as Bremsstrahlung (or braking) radiation, which is caused by the energy loss of the X-rays as they enter the metal. This is often called 'white radiation' as it is emitted over the full wavelength range. On top of the braking radiation are sharp lines generated by the quantized transition. The labels describe which orbital the decaying electron has come from, the orbital being filled and the spin state of the electron.

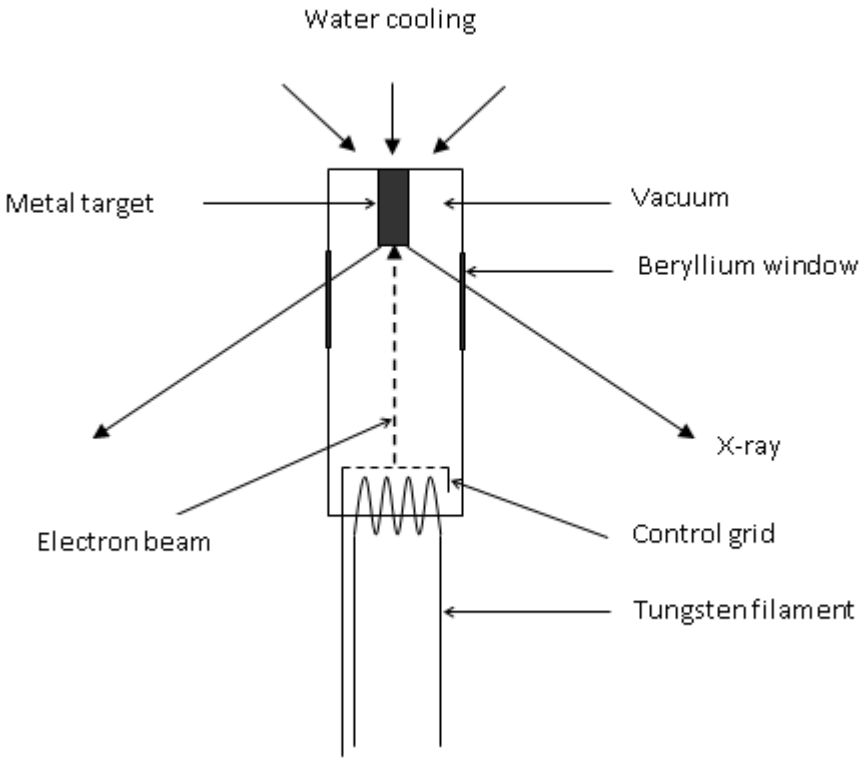

Fig 2.1 schematic diagram of X-ray tube

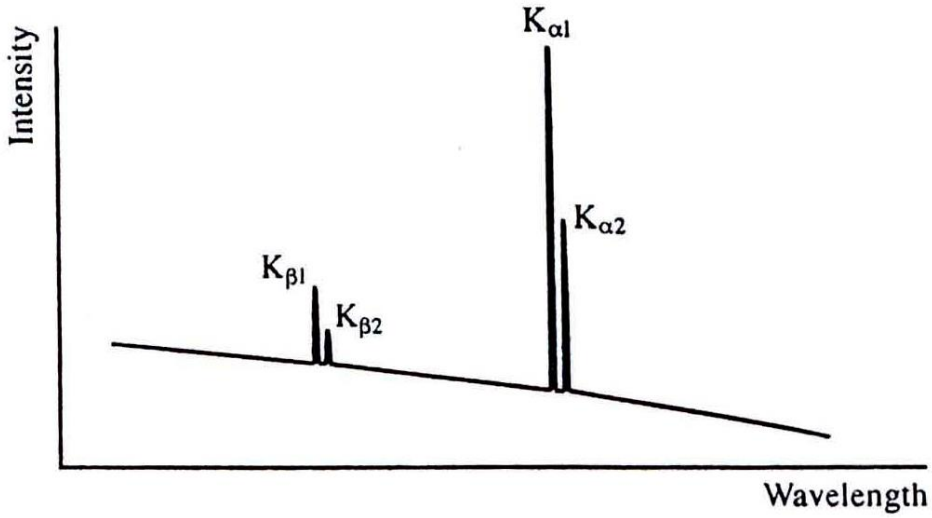

Fig 2.2 Output from an X-ray tube

2.2.3 X-ray Experiment

A single wavelength must be selected from the output from the tube to carry out the X-ray experiment. Simple filtering can get rid of some of the unwanted X-rays; for example, by using a film consisting of a metal with atomic number one below that of the metal target, the K_β lines and the white radiation can be removed. However, to obtain a single wavelength a single crystal monochromator is used. This utilizes Braggs Law to select a single wavelength. Generally the $\alpha_1$line is selected, if possible, as it has the greatest intensity.

Once a single wavelength has been selected, the beam is collimated by passing it through a slit to remove wavelengths other than the desired one, before interaction with the sample and, finally, detection of the scattered X-rays.

2.2.4 Miller Indices

X-rays interact with planes of atoms in the three-dimensional lattices which show the translational symmetry of the structure. Each plane is a representative member of a parallel set of equally spaced planes, and each lattice point must lie on one of the planes.

The labels used for describing these planes are known as Miller indices and are given the descriptions *h, k* and *l,* where *h, k, l take values of positive or negative integers or zero.* Consider the two planes shown in Fig 2.3. The Miller indices of these two members of a family of planes are given by the reciprocals of the fractional intercepts *h, k, l* along each of the unit cell directions, *i.e.* cutting at *alh, blk* and *cll.* So the 2, 8, 1 plane would cut one half of the way along *a,* one eighth of the way along *b* and all the way along *c.* The parallel plane on the diagram has the same Miller indices as it stretches across two unit cells, this time cutting the axes at *a, b/*4 and 2*c*, respectively. For planes which are parallel to one of the unit cell directions the intercept is at infinity, and therefore the Miller index for this axis is zero. The separation of the planes is known as the *d*-spacing and is normally denoted d_{hkl}. From the diagram, it is apparent that this also the perpendicular distance from the origin to the plane.

2.3 Scattering from Crystalline Solids and the Bragg Equation

The scattering of X-rays from a set of planes defined by the Miller indices *h,k,l* is shown in Fig 2.4. In order to observe useful data from the X-ray experiment the scattered X-ray beam from the points X and Z must produce diffracted beams which are in phase. This is only possible if the extra distance travelled by the X-ray photon from W to X and X to Y is an *integral number of wavelengths.* The path difference is dependent on both the lattice spacing d_{hkl} and the angle of incidence of the X-ray beam, θ :

$$\text{Path difference} = WX + XY = 2d_{hkl} \sin\theta = n\lambda \qquad (2.1)$$

where *n* is an integer, and λ is the X-ray wavelength. This equation is the Bragg equation. The *n* is normally dropped (i.e. treated as 1), as higher order (*n* = 2, etc.) diffraction maxima are just equivalent to diffraction from the *n* =1 set but at shorter *d* spacing.

In any crystalline material an infinite set of planes exists with different Miller indices, and each set of planes has a particular separation. For any set of planes there will be a diffraction maximum at a particular angle, *θ*. By combining the equation relating d_{hkl} to the lattice parameter for a particular system with the Bragg equation, a direct relationship between the diffraction angle and the lattice parameters can be derived. For example, for a cubic system, combining the geometric equation for a cubic system (where *a* is the lattice parameter):

$$\frac{1}{d^2} = \frac{h^2 + k^2 + l^2}{a^2} \qquad (2.2)$$

with the Bragg equation

$$n\lambda = 2d \sin\theta \qquad (2.3)$$

where *n* =1 and rearranging for *d* gives

$$\frac{1}{d} = \frac{2\sin\theta}{\lambda} \qquad (2.4)$$

which means

$$\frac{1}{d^2} = \frac{4\sin^2\theta}{\lambda^2} \qquad (2.5)$$

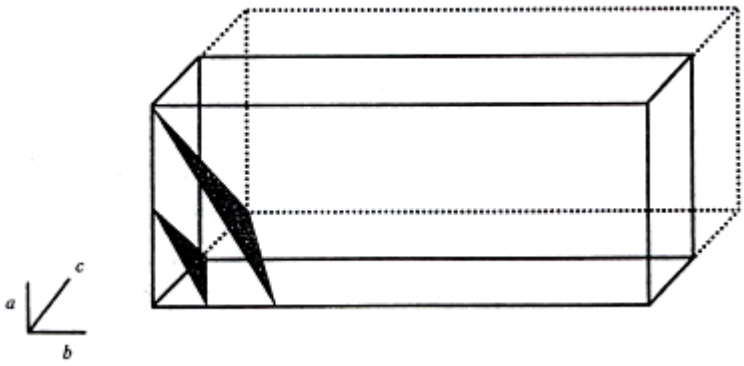

Fig 2.3 Representation of the 281 family of planes

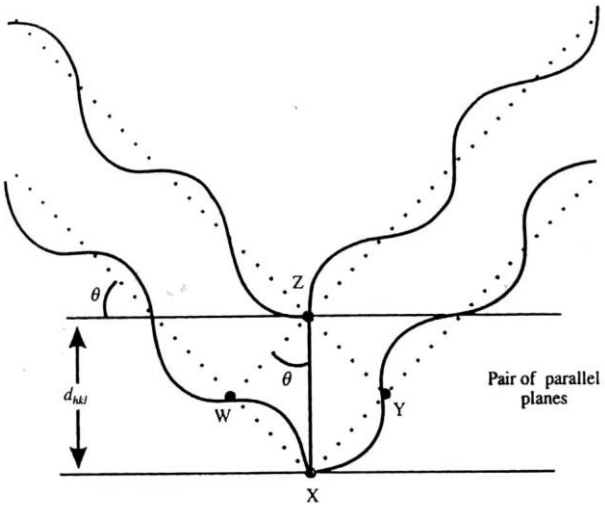

Fig 2.4 Scattering of X-rays from a parallel set of planes

Substituting for $1/d^2$ in the first equation and rearranging gives

$$\sin^2\theta = \frac{\lambda^2}{4a^2}(h^2 + k^2 + l^2)\,. \qquad (2.6)$$

By using this equation, *structural* information about the crystals under study can be obtained.

2.4 Single Crystal Diffraction

By far the dominant technique in solid state / materials chemistry is powder diffraction since single crystals are often difficult to synthesize and not representative of the bulk, which can show non-stoichiometry and disorder. However, for definitive characterization of physical properties such as magnetic ordering or electron transport, single crystals are often used, as the directional properties of these processes are lost in a polycrystalline sample. The preparation of single crystals from solid state materials is rather different from the preparation of single crystals from molecular systems.

2.5 Powder Diffraction

In a single crystal experiment the alignment of the crystal, source and detector have to be correct to observe any reflections, as scattering from one particular plane at a time is measured by aligning the crystal appropriately. In contrast, a powdered sample contains an enormous number of very small crystallites, typically 10^{-7}-10^{-4} m in sizes, which randomly adopt the whole range of possible orientations. Therefore, when an X-ray beam strikes a powdered (often termed polycrystalline) sample, it is diffracted in all possible directions (as governed by the Bragg equation) simultaneously. Each lattice spacing in the crystal gives rise to a cone of diffraction, as shown in Fig 2.5. Each cone is a set of closely spaced dots, where each dot represents diffraction from a single crystallite within the sample. With a large number of crystallites, these join together to form a continuous cone.

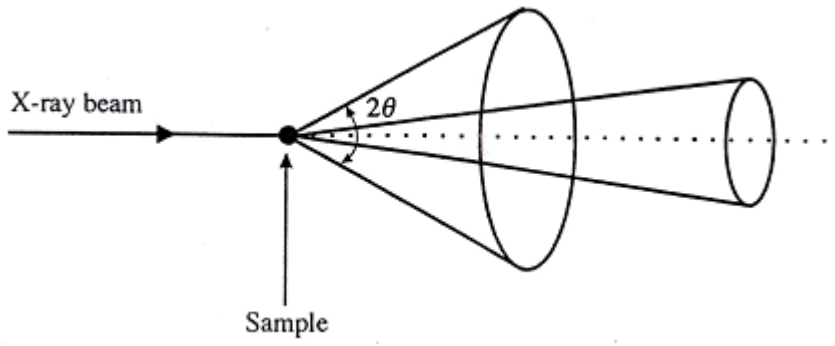

Fig 2.5 Continuous diffraction cone derived from scattering from a polycrystalline sample

2.6 Practical Aspects of the Method

Most laboratory powder X-ray diffractometers use a sealed X-ray tube with a target of copper, molybdenum, or some other metal. About half of the X-rays from such a tube are in the characteristic K_α line ($\lambda = 1.54$ Å for Cu, $\lambda = 0.07$ Å for Mo), and the remainder are in other lines and in a continuous Bremsstrahlung spectrum.

There are a large number of detectors suitable for powder X-ray diffraction. Perhaps the simplest is photographic film, which allows the collection of an entire diffractogram at one time and, with proper procedures, can be used to obtain quantitative intensities with a dynamic range up to 100 : 1 (Klug and Alexander). The simplest electronic detector, the Geiger counter, is no longer widely used because of its rather long dead time, which limits the maximum count rate. The gas-filled proportional counter offers higher count rates and some degree of X-ray energy resolution. The most widely used X-ray detector today is the scintillation counter, in which X-rays are converted into visible light, typically in a thallium-doped NaI crystal, and then into electronic pulses by a photomultiplier tube. Various semiconductor detectors [Si(Li), positive-intrinsic-negative (PIN)] offer energy resolutions of 100 eV to 300 eV, sufficient to distinguish fluorescence from different elements and from the diffracted X-rays, although their count rate capability is generally lower than that of scintillation counters.

Some of the most important configurations for X-ray powder diffraction instruments are illustrated in Fig 2.6. The simple Debye-Scherrer camera in (a) records a wide range of angles on curved photographic film but suffers from limited resolution. Modem incarnations include instruments using curved position- sensitive detectors and imaging plates and are in use at several synchrotron sources. It generally requires a thin rod-shaped sample either poured as a powder into a capillary or mixed with an appropriate binder and rolled into the desired shape. The Bragg-Brentano diffractometer illustrated in (b) utilizes parafocusing from a flat sample to increase the resolution available from a diverging X-ray beam; in this exaggerated sketch, the distribution of Bragg angles is 3°, despite the fact that the sample subtends an angle of 15° from source or detector.

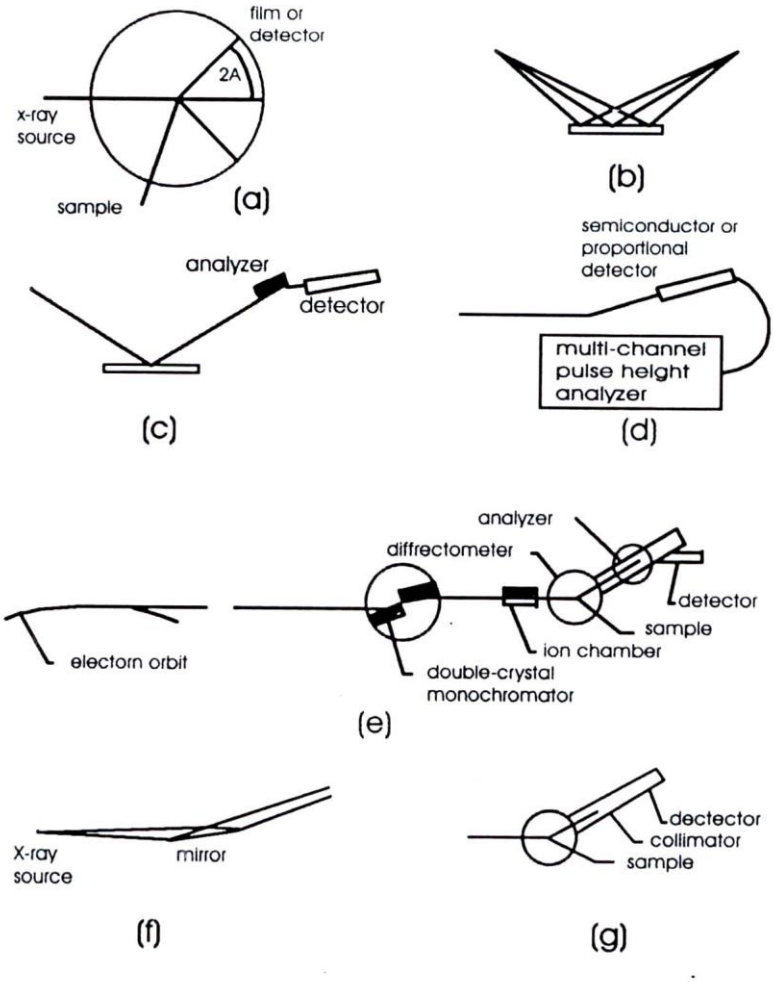

Fig 2.6 Schematic illustrations of experimental setup for powder diffraction measurements

The addition of a diffracted-beam monochromator illustrated in (c) produces a marked improvement in performance by eliminating X-ray fluorescence from the simple. For high-pressure cells, with limited access for the X-ray beam, the energy-dispersive diffraction approach illustrated in (d) can be an attractive solution. A polychromatic beam is scattered through a fixed angle, and the energy spectrum of the diffracted X-rays is converted to *d* spacing for interpretation.

There are a number of sources of background in a powder diffraction experiment. X-rays can be scattered from the sample by a number of mechanisms other than Bragg diffraction: Compton scattering, thermal diffuse scattering, scattering by defects in the crystal lattice, multiple scattering in the sample, and scattering by noncrystalline components of the sample, by the sample holder, or even by air in the X-ray beam path. The X-rays scattered by all of these mechanisms will have an energy that is identical to or generally indistinguishable from the primary beam, and so it is not possible to eliminate these effects by using energy–sensitive detectors. Another important source of background is X-ray fluorescence, the emission of X-rays by atoms in the target that have been ionized by the primary X-ray beam. X-ray fluorescence is always of a longer wavelength (lower energy) than the primary beam and so can be eliminated by the use of a diffracting crystal between sample and detector or an energy–sensitive detector (with the precaution that the fluorescence radiation does not saturate it) or controlled by appropriate choice of the incident wavelength.

2.7 Data Analysis and Interpretation

A very important technique for analysis of powder diffraction data is the whole-pattern fitting method proposed by Rietveld. It is based on the following properties of X-ray (and neutron) powder diffraction data: a powder diffraction pattern usually comprises a large number of peaks, many of which overlap, often very seriously, making the separate direct measurement of their integrated intensities difficult or impossible. However, it is possible to describe the shape of a Bragg peaks in the pattern by a small (compared to the number of peaks) number of profile parameters. This allows the least-squares refinement of an atomic model combined with an appropriate peak shape function, i.e., a simulated powder pattern,

directly against the measured powder pattern. This may be contrasted to the single-crystal case, where the atomic structure is refined against a list of extracted integrated intensities.

The parameters refined in the Rietveld method fall into two classes: those that describe the shape and position of the Bragg peaks in the pattern (profile parameters) and those that describe the underlying atomic model (atomic or structural parameters). The former include the lattice parameters and those describing the shape and width of the Bragg peaks. In X-ray powder diffraction, a widely used peak shape function is the Pseudo-Voigt function *Thompson exal,* a fast-computing approximation to a convolution of a Gaussian and a Lorentzian (Voigt function). It uses only five parameters (usually called *U, V, W, X and Y*) to describe the shape of all peaks in the powder pattern. In particular, the peak widths are a smooth function of the scattering angle 2θ. Additional profile parameters are often used to describe the peak asymmetry at low angles due to the intersection of the curved Debye-Scherrer cone of radiation with a straight receiving slit and corrections for preferred orientation. The structural parameters include the positions, types, and occupancies of the atoms in the structural model and isotropic or anisotropic thermal parameters (Debye-Waller factors). The power of the Rietveld method lies in simultaneous refinement of both profile and atomic parameters, thereby maximizing the amount of information obtained from the powder data.

2.8 Sample Preparation of XRD Measurement

The preparation of samples to avoid unwanted artifacts is an important consideration in powder diffraction experiments. One issue is that preferred orientation (texture) should be avoided or controlled. The grains of a sample may tend to align, especially if they have a needle or plate like morphology, so that reflections in certain directions are enhanced relative to others. Various measures such as mixing the powder with a binder or an inert material chosen to randomize the grains or pouring the sample sideways into the flat plate sample holder are in common use. It is also possible to correct experimental data if one can model the

distribution of crystallite orientations; this option is available in most common Rietveld programs.

However, grinding can introduce strain broadening into the pattern, and some experimentation is usually necessary to find the optimum means of preparing a sample. A useful test of whether a specimen in a diffractometer is sufficiently powdered is to scan the sample angle θ over several degrees while leaving 2θ fixed at the value of a strong Bragg peak, in steps of perhaps 0.01^{o} ; fluctuations of more than a few percent indicate trouble. It is good practice to rock (flat plate) or twirl (capillary) the sample during data collection to increase the number of observed grains.

In as much as a powder diffraction experiment consists of “simply” measuring the diffracted intensity as a function of angle, one can classify sources of systematic error as arising from measurement of the intensity or the angle or from the underlying assumptions. Errors of intensity can arise from detector saturation, drift or fluctuations of the strength of the X-ray source, and the statistical fluctuations intrinsic to counting the random arrival of photons.

Error of the angle can arise from mechanical faults or instability of the instrument or from displacement of the sample from the axis of the diffractometer (parallax). A subtle form of parallax can occur for flat-plate samples that are moderately transparent to X-rays, because the origin of the diffracted radiation is located below the surface of the sample by a distance that depends on the diffraction angle. Another effect that can give rise to an apparent shift of diffraction peaks is the asymmetry caused by the intersection of the curved Debye-Scherrer cone of radiation with a straight receiving slit. This geometric effect has been discussed by several authors and it can produce a significant shift in the apparent position of low-angle peaks if fitted with a model lineshape that does not properly account for it. So that the observed Bragg angle is slightly shifted for it. So that the observed Bragg angle is slightly shifted from its value inside the sample.

There are a number of standard samples that are useful for verifying and monitoring instrument performance and as internal standards. Silver behenate powder has been proposed as a useful standard with a very large lattice spacing of c = 58.4 Å.

2.9 Comparison Against a Database of Known Materials

An ongoing investigation of novel carbon materials yielded a series of samples with new and potentially interesting properties: (1) the strongest signal in a mass spectrometer was shown to correspond to the equivalent of an integer number of carbon atoms, (2) electron diffraction indicated that the samples were at least partially crystalline, and (3) while the material was predicted to consist entirely of carbon, the procedures for synthesis and purification had involved an organic Li compound. The Powder Diffraction File (PDF) database provided by the International Center for Diffraction Data (ICDD, 1998) allows for searching based on several search criteria, including types of atoms, positions of Bragg peaks, or unit cell parameters. Note that it is not necessary to know the unit cell of a compound to search the database against its diffractions pattern, nor is it necessary to know the crystal structures (or even the unit cells) of all the compounds included in the database.

Searches for materials with an appropriate position of their strong diffraction peaks containing C only, or containing some or all of C, N, O, or H, did not result in any candidate materials. The peak intensities listed in the database, converted to 2θ for the appropriate wavelength. This type of experiment is fairly simple, and both data collection and analysis can be performed quickly. Average sample quality is sufficient, and usually so are relatively low-resolution data from an X-ray tube. In fact, this test is routinely performed before any attempt to solve the structure of an unknown and presumably new material.

2.10 The Determination of Crystal Structure

The Determination of an unknown structure proceed in three major steps:

(i) The shape and size of the unit cell are deduced from the angular positions of the diffraction lines. An assumption is first made as to which of the seven crystal systems the unknown structure belongs to, and then, on the basis of this assumption, the correct Miller indices are assigned to each reflection. This step is called “indexing the pattern” and is only possible when the correct choice of crystal system has been made. Once this is done, the shape of the unit cell is known (from the crystal system), and its size is calculable from the position and Miller indices of the diffraction lines.

(ii) The number of atoms per unit cell is then computed from the shape and size of the unit cell the chemical composition of the specimen, and its measured density.

(iii) Finally, the positions of the atoms within the unit cell are deduced from the relative intensities of the diffraction lines.

Only when these steps have been accomplished is the structure determination complete. The third step is generally the most difficult, and there are many structures which are known only incompletely, in the sense that this final step has not yet been made. Nevertheless, knowledge of the shape and size of the unit cell, without any knowledge of the atom positions, in itself of very great value in many applications.

Knowledge of the crystal structure permits determination of the coordination number (the number of nearest neighbours) for each kind of atom or ion, calculation of interatomic distances, and elucidation of other structural features related to the nature of chemical bonding and the understanding of physical properties in the solid state. A perfect crystal constitutes the repetition of a single very small unit of structure called the unit cell, in a regular way so as to fill the volume occupied by the crystal.

A crystal may for some purposes be described in terms of a set of three crystal axes *a, b* and *c*, which may or may not be equal length for a right angles, depending on the symmetry of the crystal. These axes from the basis for a coordinate system with

which the crystal may be described. An important property of crystals, known at least a century before the discovery of X-rays, is that for any crystal the crystal axes can be so chosen that all crystal faces can be described by equations of the form

$$hx + ky + lz = \text{positive constant} \qquad (2.7)$$

where x, y and z are the coordinates of any point on a given crystal face, in a coordinate system with axes parallel to the assigned crystal axes and with units equal to the assigned axial lengths a, b, c; and where *h, k,* and *l* are small integers, positive, negative, or zero. This is known as the *law of rational indices.* The integers *h, k,* and *l* are known as the Miller indices, and when used to designate a crystal face are ordinarily taken relatively prime (i.e., with no common integral factor). Each crystal face may then be designated by three Miller indices *hkl,* as shown in Fig 2.7 and also show the law of rational indices historically formed the strongest part of the evidence supporting the conjecture that crystals are built up by repetition of a single unit of structure.

The crystal axes for a given crystal may be chosen in many different ways; however, they are conventionally chosen to yield a coordinate system of the highest possible symmetry. It has been found that crystals can be divided into seven possible systems on the basis of the highest possible symmetry that the coordinate system may possess as a result of the symmetry of the crystal. This symmetry is best described in terms of symmetry restrictions governing the values of the axial lengths *a, b,* and *c* and the interaxial angle and α, β , and γ . The crystal systems are as follows:

(1) **Triclinic system**: No restriction.

(2) **Monoclinic system**: No restriction on lengths *a, b, c* ; however $\alpha = \gamma = 90^{o}$; $\beta \neq 90^{o}$.

(3) **Orthorhombic system**: Non restriction on *a, b, c* ; however $\alpha = \beta = \gamma = 90^{o}$.

(4) **Tetragonal system**: a = b $\neq$ c; $\alpha = \beta = \gamma = 90^{o}$.

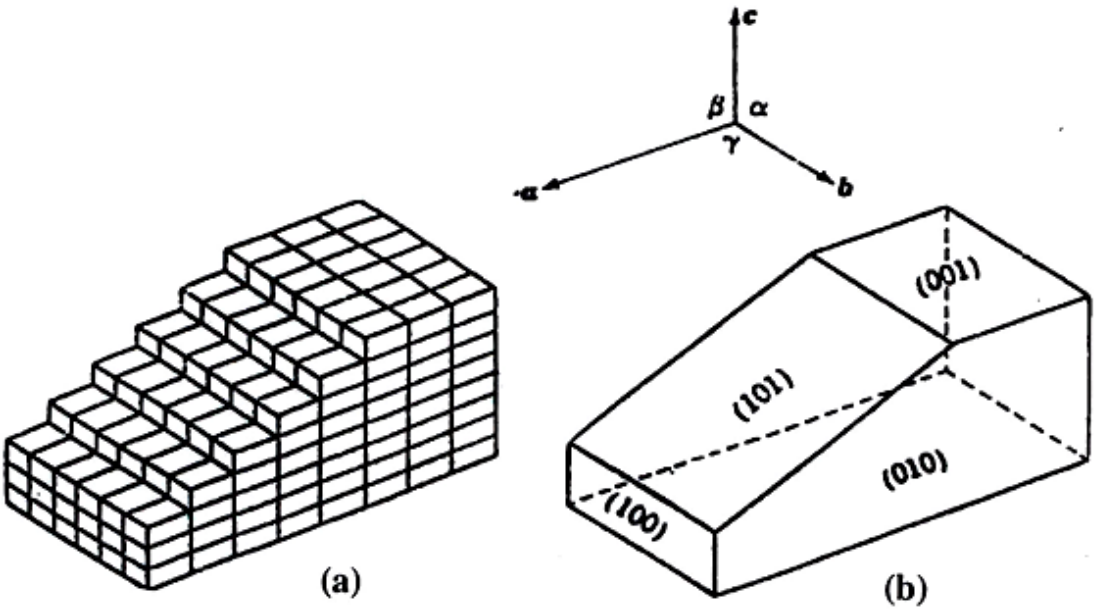

Fig 2.7 (a) Schematic diagram of a crystal, showing unit cells

(b) same crystal, showing axes and Miller indices

(5) **Hexagonal system**: *Hexagonal division* a = b = b' ≠ c ; $\alpha = \beta = \gamma = 90^o$; $\gamma = \gamma' = 120^o$ (there being three axes *a, b, and b*' in the basal plane at 120^o angular spacing; the b' axis is redundant).

(6) **Rhombohedral division**: $a = b = c$: $\alpha = \beta = \gamma = 90^o$ (Although the coordinate systems in these two divisions are of different symmetry, hexagonal axes may be used in the description of rhombohedral crystals and vice versa.)

(7) **Cubic system**: $a = b = c$; $\alpha = \beta = \gamma = 90^o$ (Cartesian coordinates).

The symmetry of a crystal is not completely specified. However, by naming the crystal system to which it belongs, each crystal system is further subdivided into *crystal classes,* of which there are 32. On the basis of the detailed symmetry of the atomic structure of crystals, further subdivision is possible.

Since a crystal structure constitutes a regular repetition of a unit of structure and it is periodic in three dimensions. The periodicity of a crystal structure may be represented by a *point lattice* in three dimensions. This is an array of points that is invariant to all the translations that leave the crystal structure invariant and to no others. To define a crystal lattice in another way, consider the crystal structure to be divided into unit cells (parallelepipeds in shape) in such a way as to obtain the smallest unit cells possible. These unit cells are then called *primitive.* Starting with a set of crystal axes that are parallel to three edges of a unit cell and equal to them in length, a point lattice may be defined as the infinite array coordinates *xyz* of which assume all possible combinations *mnp* of integral values (positive, negative, and zero), and only integral values. There is then one lattice point per unit cell.

It is frequently found that it is not possible to find a primitive unit cell with edges parallel to crystal axes chosen on the basis of symmetry. In such a case the crystal axes, chosen on the basis of symmetry, are proportion edges of a unit of structure those larger than a primitive unit cell. Such is called a *non-primitive* unit cell and there is more than one lattice point non-primitive unit cell. If the non-primitive unit cell is chosen as small as possible consistent with the symmetry desired it is found that the extra lattice points (those other than the corner points) lie in the center of

the unit cell or at the centers of some or all of the faces of the unit cell. The coordinates of the lattice points are, therefore, of the unit cell.

Within a given crystal system there are in some cases several different types of crystal lattice, depending upon the type of minimum-size unit cell that corresponds to a choice of axes appropriate to the given crystal system. This unit cell may be primitive of in certain cases *body centered I, face-centered F,* or *end-centered A, B* and *C* depending on which pair of end faces of the unit cell is centered. These lattices are designated as primitive, body-centered, face-centered or end-centered. There are in all 14 types of lattice, known as Bravais lattices. In the cubic system there are three: primitive, body-centered, and face-centered: these are shown in Fig 2.8.

2.11 The Determination of Lattice Type

From the angle at which X-rays are diffracted by a crystal it is possible to deduce the interplanar distances d. To 0determine the lattice type and, compute the unit-cell dimensions, it is necessary to deduce the Miller indices of the planes that show these distances. In the case of powder specimen (where all information concerning orientations of crystal axes has, been lost) the only available information. Regarding Miller indices is that obtainable by application of the following.

For cubic system,

$$d = \frac{a_0}{\sqrt{h^2 + k^2 + l^2}} = \frac{a_0}{\mathrm{M}} \tag{2.8}$$

$$M^2 = h^2 + k^2 + l^2 \tag{2.9}$$

To find which of the three types of cubic lattice is the correct one, we make use of some interesting properties of integers. From Eqn (2.9) we see that

$$\left(\frac{1}{d}\right)^2 = \left(\frac{1}{a_0}\right)^2 \mathrm{M}^2 = \left(\frac{1}{a_0}\right)^2 (h^2 + k^2 + l^2) \tag{2.10}$$

so that, if we square our reciprocal spacing, it should be possible to find a numerical factor which will convert them into a sequence of integers, which we shall find convenient to make relatively prime.

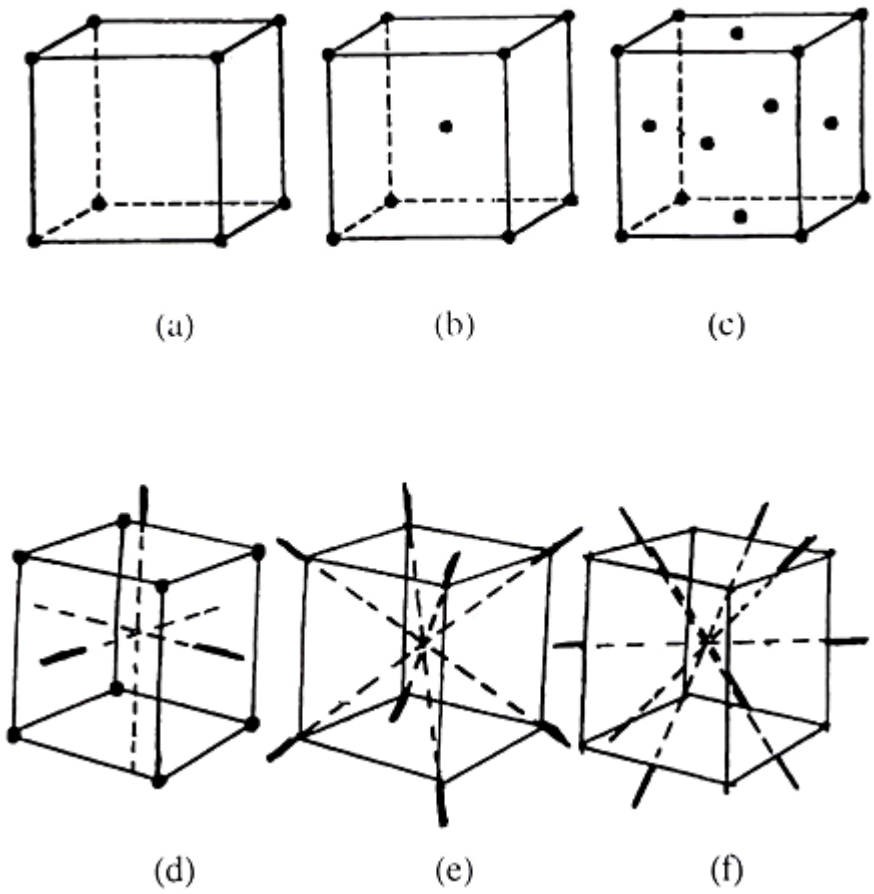

Fig 2.8 The cubic space lattices and symmetry axes for the conventional cells (a) primitive, *P* (b) body-centered, *I* (c) face-centered, *F* (d) the three triad axes (e) the four traid axes and (f) the six diad axes

The proper set of integers satisfying Equation

$$\frac{\sin^2\theta}{(h^2+k^2+l^2)} = \frac{\sin^2\theta}{\mathrm{s}} = \frac{\lambda^2}{4a^2} \tag{2.11}$$

cannot be found, then the substance involved does not belong to the cubic system, and other possibilities (tetragonal, hexagonal, etc) must be explored. Also determine the Bravais Lattice of the specimen by observing which lines present and which are absent. There is one difficulty that may arise in the interpretation of cubic powder patterns, and that is due to possible ambiguity between simple cubic and body-centered cubic patterns. There is a regular sequence of lines in both patterns up to the sixth line; the sequence then continues regularly in body-centered cubic patterns, but is interrupted in simple cubic patterns since $S = 7$ is impossible. For example, supposed that the substance involved is actually body-centered cubic but the investigator mistakenly indexes it as simple cubic, as signing the value $S = 1$ to the first line, $S = 2$ to the second line, …etc. He thus offerings a value of $\lambda^2/4a^2$ twice as large as the true one and a value of 'a' which is $1/\sqrt{2}$ times the true one. This sort of difficulty can be avoided simply by choosing a wavelength short enough to produce at least seven lines on the pattern.

CHAPTER III

MOLECULAR VIBRATIONS

Analysis of the internal motions of a crystal relies heavily upon the symmetry properties of the crystal, which are well treated on the basic group theory. The determinations of the number of vibrational modes, their symmetries and hence the selection rules for Raman scattering or IR absorption, may be carried out in the same general manner as for free molecules, bearing in mind a few differences to be discussed and the absence of rotational and translational freedom to be discussed for the unit cell. The purpose of this chapter is to present the basic group theoretical methods with may be employed to determine crystal selection rules, to illustrate the method in KH_2PO_4 crystal and to present a set of tables organized to facilitate rapid vibrational selection rule determination [2, 4, 8, 14].

3.1 Factor Group Analysis

In the development of the properties of the translation group, the lattice was constructed entirely of points, the internal structure of individual primitive cells have been ignored. However, the symmetry of the lattice with a basis, that is, one whose primitive cell contains, in general, a number of atoms, is further specified by the operations of the factor group. As shown above, potentially infrared or Raman-active vibrations correspond to the totally symmetric representation of the translation groups, for which $k = 0$. Hence, for spectroscopic purposes only those representations of the space group, which are derived from the irreducible representations of the factor group, need be considered.

The atoms within a unit cell are related by the familiar point group symmetry operations in addition to screw axis and glide planes. A screw axis symmetry operation is a rotation followed by a translation along the axial direction. A glide plane operation is a reflection across the plane followed by a translation along the plane. By thus separating out the translations, a finite group remains, which is a factor group of the space group and which describes the symmetry of a unit cell.

3.2 Molecular Vibrations

In molecular spectroscopy we observe transition between quantized states by studying the interaction between the sample and electromagnetic radiation. Molecules exhibit incredibly complex vibrational patterns, but these motions are linear combinations of much simpler fundamental modes of vibration. A mode of vibration in a molecule is a periodic contortion in which the centers of mass of the molecular or its orientation do not change as a result of the vibration and all of the atoms pass through their equilibrium position coincidentally.

The position of a molecule in three dimensional space can be described by using an x, y and z co-ordinate for each atom. Thus, for a molecule comprised of n atoms $3n$ co-ordinates are required to describe its shape, position and orientation. The motion of each atom can be described by a change Δx, Δy and Δz in these coordinates. There are $3n$ fundamental distinct molecular motions which are called degrees of freedom, and any other motion is some linear combination of these. Molecular motions consist of translations, rotations and vibrations, but predominantly mixtures of all three.

In consideration of molecular vibrations, movements consisting solely of translations or pure rotations must be ignored. Three of the degrees of freedom represent the translation of the whole molecule along the x, y or z axis. Translation in any other direction can be resolved into displacements along these three Cartesian axes. A nonlinear molecule also has three pure rotations about these axes. A linear molecule, however, only has two distinct rotations since no rotation occurs about the molecular axis. After discounting pure rotations and translations we are left with motions which must involve vibration. Thus non-linear molecule possess $3n$-6 fundamental as whilst a linear molecule has $3n$-5.

Many characteristics of molecular vibrations can be understood in terms of classical simple harmonic motion. A diatomic molecule can be viewed naively as point masses connected by a spring as shown in Fig 3.1. To displace the masses from their equilibrium position requires the application of a force, F.

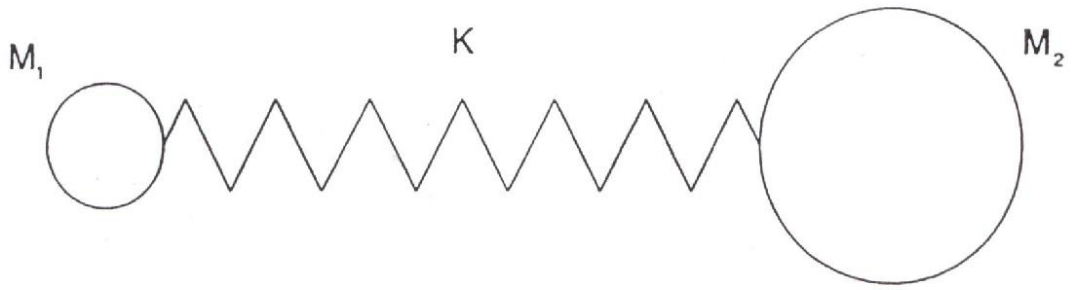

Fig 3.1 A molecule can be viewed as point masses connected by weightless springs

For simple harmonic system, $F = kx$, where x is the displacement (in meters) and k is the force constant (N/m). This is a statement of Hooke's law. This simple mechanical system will vibrate at a frequency given by;

$$\nu_{\text{vib}} = \frac{1}{2\pi}\sqrt{\frac{k}{\mu}} \tag{3.1}$$

where μ is the reduced mass

$$\mu = \frac{m_1 m_2}{m_1 + m_2}\,\text{kg} \tag{3.2}$$

This equation actually allows us to predict vibrational frequencies for diatomic molecules very well. The potential energy function for a harmonic oscillator is a parabola as shown in Fig 3.2. However, although simple harmonic motion is a reasonable approximation to molecular behaviour, the potential function derived from it would never allow chemical bonds to break. The simple harmonic oscillator is only a model; real molecules are anharmonic vibrators. A more realistic model for the potential energy function is given by the Morse function.

$$E = D_{eq}\,[1 - exp\{a(r_{eq} - r)\}]^2 \tag{3.3}$$

where

D_{eq} = dissociation energy

r_{eq} = equilibrium bond length

r = internuclear distance

a = constant for a particular molecule

This is shown diagrammatically in Fig 3.2. Compression or expansion of a chemical bond away from its equilibrium value is an endothermic process. The curvature of the bottom of the potential energy well is indicative of the stiffness of the bond; the steeper the well, the more rigid the vibrator. The molecular stiffness is described quantitatively, as referred to previously, by the force constant k. Although the potential energy curve is a continuous function, the total vibrational energy of a molecule is quantized, i.e. it can possess only certain discrete values.

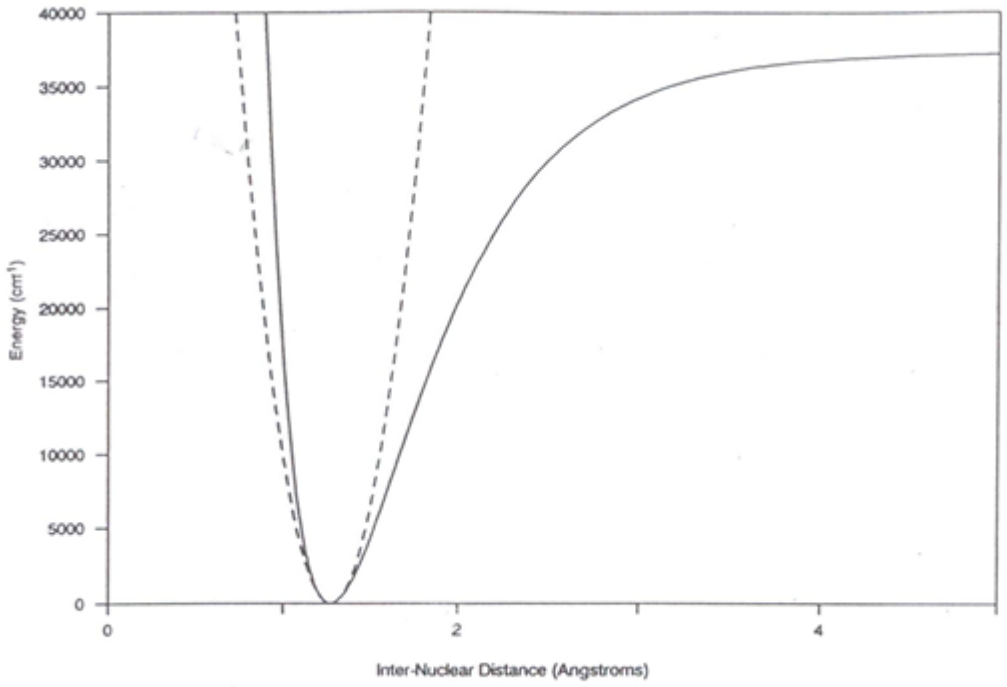

Fig 3.2 A Morse curve compared with a parabolic potential function for $^{1}H^{35}Cl$ drawn to scale

These values are described by the vibrational quantum number, *V*, which can take values *V* = 0, +1, +2, +3, +4... . The expression for the quantized vibrational energy is different, depending on whether we assume the molecule is a harmonic or an anharmonic oscillator. For a simple harmonic oscillator the expression is:

$$E_{\text{vib}} = h\,(V + ½)\,\nu_{\text{vib}} \qquad (3.4)$$

where

h = Planck's constant (J sec)

ν_{vib} = Vibrational frequency (Hz)

V_{vib} = Vibrational quantum number

The anharmonic oscillator model gives the Eqn (3.5). The energy values obtained compare well with experimental observations.

$$E_{vib} = h\left[\left(v+\frac{1}{2}\right)\nu_{vib} - \left(V+\frac{1}{2}\right)^2 X_c \nu_{vib}\right] J \qquad (3.5)$$

where

X_c = Anharmonicity constant

ν_{vib} = Vibrational frequency (Hz)

V = Vibrational quantum number

The lowest vibrational energy state is represented by V=0. It can be seen from Eqn (3.4) and Eqn (3.5) that Evib is never zero. Thus, even at absolute zero, molecules still vibrate. Another flaw in the simple harmonic model is that it predicts that the total vibrational energy levels will be equally spaced and experiment proves this not to be true. In reality the energy levels converge as V increases, reaching an asymptotal value at the dissociation limit of the oscillator, and this is correctly predicted by the anharmonic model. Fig 3.3 shows the vibrational energy level 'ladders' predicted by the two models. If we plot a graph of total vibrational energy vs interatomic separation, the allowed values for a molecule consist of a series of horizontal lines which converge at high energy. For a given quantized vibrational energy level there is a range of allowed values of internucler distance. As the vibrational quantum number increases then the amplitude of vibration also increase. This is illustrated in Fig 3.4.

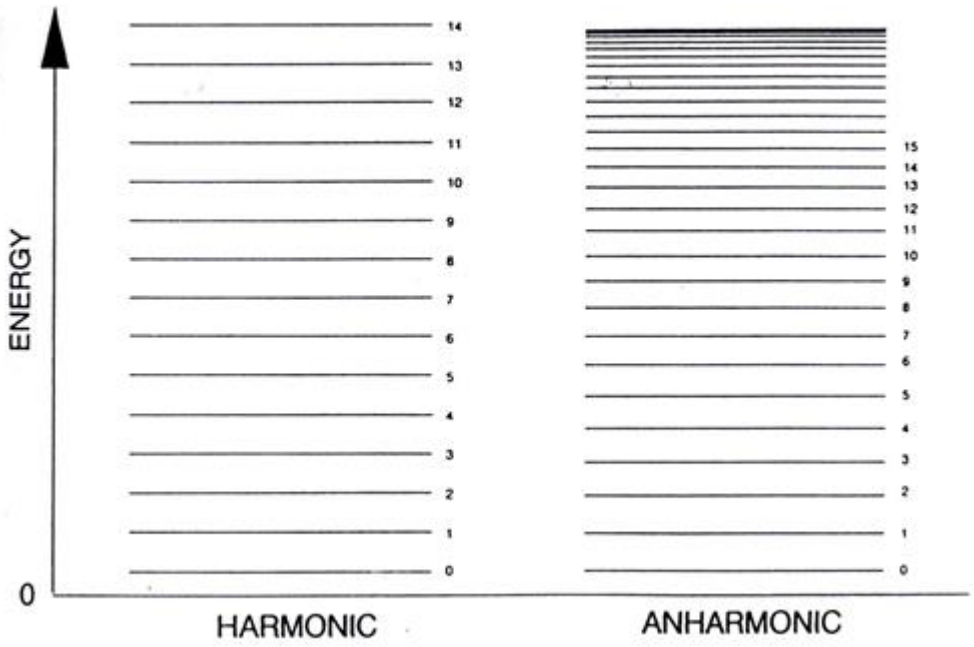

Fig 3.3 Energy level ladders for harmonic and anhamonic models. The energy levels are evenly spaced in the harmonic model, but converge when anharmonicity is considered

The total vibrational energy is composed of kinetic and potential energy, whereas the Morse curve represents only potential energy. The points of intersection between the vibrational energy levels and the Morse curve represent the classical turning point of an oscillator where all the energy is potential and none is kinetic. At intermediate values of internuclear distance, some of the energy is potential and some kinetic. The injection (or removal) of a quantum of energy, in the form of a photon, is expressed by a change in the vibrational quantum number. These changes are observed in vibrational spectroscopy.

So far we have considered only diatomic molecules. When we move on to consider a triatomic molecule such as H_2O, the vibrational behaviour is more complex, with multiple bond stretches as well as bending vibrations. In H_2O there are three atoms and hence three ($3n$-6) fundamental modes. The number of stretching vibrations is equal to the number of linkages in the molecule. The three modes of water are shown in Fig 3.5.

3.3 Raman Spectroscopy

Since the development of the laser, Raman spectroscopy has become an important method for investigating elementary excitations in solids, for example, phonons and plasmons. In this type of spectroscopy one studies the inelastic scattering of light by the elementary excitation of interest. This inelastic scattering was already mentioned in connection with scattering from phonons. As for all scattering from time-varying structures (e.g. a vibrating lattice), energy must be conserved and, to within a reciprocal lattice vector, wave vector too, i.e. we have

$$\hbar\omega_0 - \hbar\omega \pm \hbar\omega(q) = 0 \tag{3.6}$$

$$\hbar k_0 - \hbar k \pm \hbar q + \hbar G = 0 \tag{3.7}$$

where ω_0, $\boldsymbol{k}_0$ and ω, $\boldsymbol{k}$, characterize the incident and scattered light waves respectively; ω ($\boldsymbol{q}$) and $\boldsymbol{q}$ are angular frequency and the wave vector of the elementary excitation, e.g. phonon. For light in the visible region of the spectrum, $|\boldsymbol{k}_0|$ and $|\boldsymbol{k}|$ are of the order of 1/1000 of a reciprocal lattice vector, which means that only excitations in the center of the Brillouin zone ($|\boldsymbol{q}|$=0) can

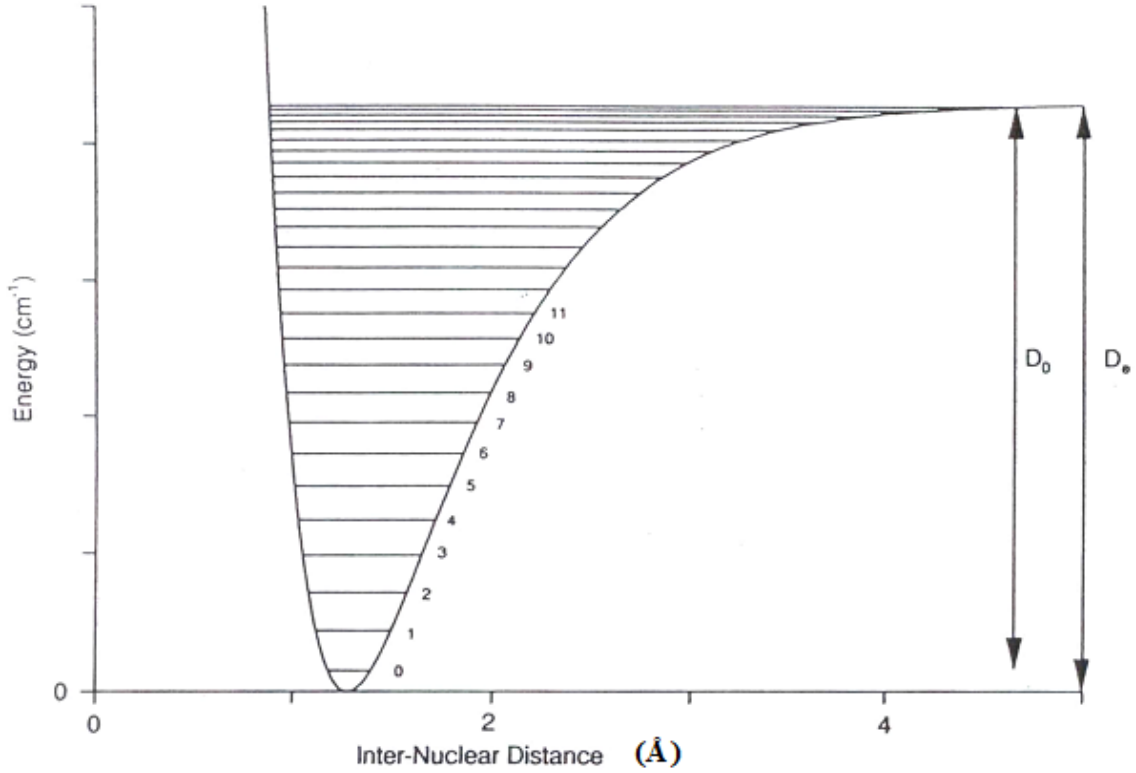

Fig 3.4 The energy level diagram for hydrogen chloride showing the allowed values of internuclear distances for each value of the vibrational quantum number

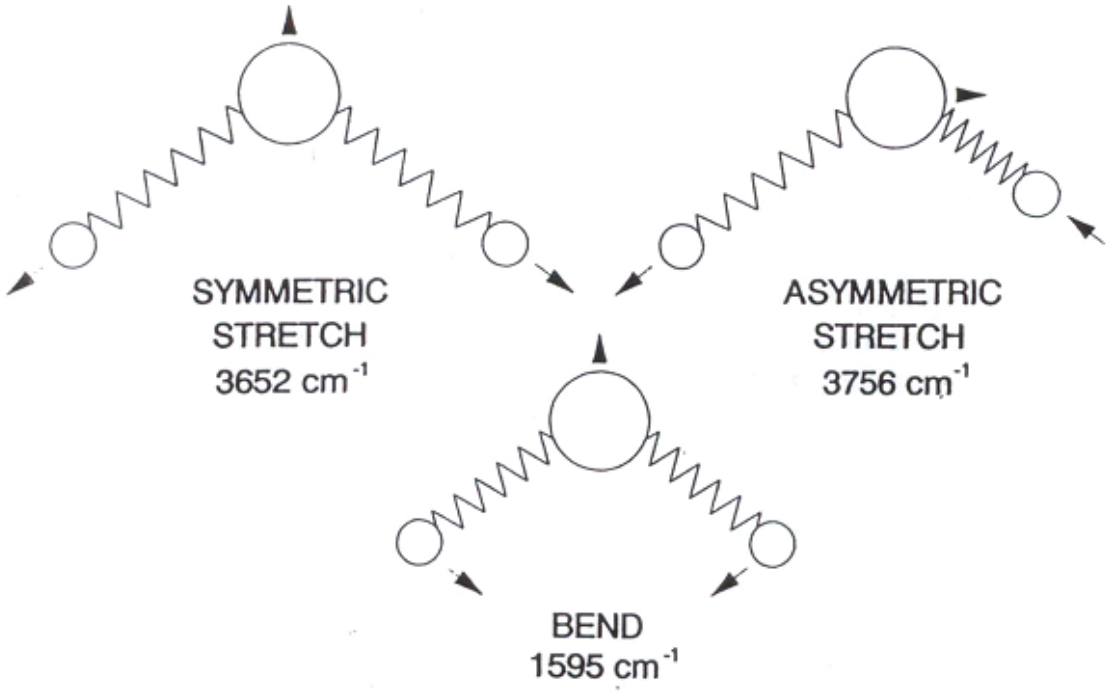

Fig 3.5 The fundamental vibrational modes of water. There are two stretching and one bending vibration.

take part in Raman scattering. The interaction of visible light with solids occurs via the polarizability of the valence electrons. The electric field E_0 of incident light wave induces, via the susceptibility tensor $\underline{\chi}$ a polarization ***P***, i.e.

$$\boldsymbol{P} = \varepsilon_0 \chi \mathrm{E}_0 \qquad \text{or} \qquad \boldsymbol{P}_i = \varepsilon_0 \sum_j \chi_{ij} E_{j_0} \tag{3.8}$$

The periodic modulation of ***P*** leads, in turn, to the emission of the wave–the scattered wave. In a classical approximation, the scattered wave can be regarded as dipole radiation from the oscillating dipole ***P***. From the laws of electrodynamics one obtains the energy flux density in direction **s** i.e. the Pointing vector **S** at distance r from the dipole as

$$\mathrm{S(t)} = \frac{\omega^4 \mathrm{P}^2 \sin^2 \theta}{16\pi^2 \varepsilon_0 \mathrm{r}^2 \mathrm{c}^3} \quad \mathrm{s} \tag{3.9}$$

Here θ is the angle between the direction of observation $\hat{\mathrm{s}}$ and direction of the variation of ***P***. The electronic susceptibility χ is Eqn (3.8) is now a function of the nuclear coordinates and thus of the displacement associated with the lattice vibration $X[\omega(\boldsymbol{q}), \boldsymbol{q}]$. Similarly, χ can also be a function of some other collective excitations $X[\omega(\boldsymbol{q}), \boldsymbol{q}]$, for example the density of vibrations associated with a longitudinal electron plasma wave of the traveling-wave-like vibrations of magnetization an in otherwise perfectly ordered ferromagnet (magnons). These "displacement" can be regarded as perturbations and in a formal expansion in X it suffices to retain the first two terms:

$$\chi = \chi^0 + (\partial\chi / \partial \mathrm{X})\mathrm{X} \tag{3.10}$$

As we only need to consider excitations with $\boldsymbol{q} \approx 0$ we can simply matters by writing $\boldsymbol{X} = \boldsymbol{X}_0 \cos [\omega(\boldsymbol{q})\, \boldsymbol{t}]$ and, if the electric field E_0 of the incident wave is described by $E_0 = \hat{E}_0 \cos \omega_0 t$, we obtain from Eqn (3.8) the polarization appearing in Eqn (3.9) as

$$P = \varepsilon_0 \chi^0 \hat{\mathrm{E}}_0 \cos \omega_0 t + \varepsilon_0 (\partial\chi / \partial \mathrm{X})\, \mathrm{X}^0 \hat{\mathrm{E}}_0 \cos [\omega_0 (q).\, t] \cos \omega_0 t$$

$$P = \varepsilon_0 \chi^0 \hat{\mathrm{E}}_0 \cos\omega_0 t + \tfrac{1}{2} \varepsilon_0 (\partial\chi/\partial \mathrm{X})\, \mathrm{X}^0 \hat{\mathrm{E}}_0 \cos [\omega + \omega(q).t] + \cos[\omega_0 - \omega(q)]t \tag{3.11}$$

The scattered radiation expressed by Eqn (3.8) therefore contains, along with the elastic contribution of the frequency ω_0 (the Rayleigh scattering), further terms

known as Raman side bands with the frequencies $\omega_0 \pm (\boldsymbol{q})$ shown in Fig 3.6 (a) and (b). The plus and minus signs correspond to scattered light quanta that have, respectively, absorbed the energy of, and lost energy to, the relevant elementary excitation $[\omega(\boldsymbol{q})\boldsymbol{t}]$. The lines with frequency smaller than ω_0 are called the Stokes lines; those with higher frequency are the anti-Stokes lines. For the latter lines to be present it is necessary that the elementary excitation, e.g. phonon, is already excited in the solid. Thus at low temperatures the intensity of the anti Stokes lines is much reduced because the relevant elementary excitation is largely in its ground state. The intensity of the inelastically scattered radiation is typically a factor of 10^6 weaker than that of primary radiation.

The susceptibility, χ , must relate one vector, the electrical field, to another vector, the induced dipole moment, where these two vectors are not necessarily parallels. In general, a tensor which involves nine numbers is required for this Eqn (3.12), and it is a 3x3 matrix.

$$\boldsymbol{P} = \varepsilon_0 \chi E_o$$

$$\begin{pmatrix} P_x \\ P_y \\ P_z \end{pmatrix} = \varepsilon_0 \begin{pmatrix} \chi_{oxx} & \chi_{oxy} & \chi_{oxz} \\ \chi_{oyx} & \chi_{oyy} & \chi_{oyz} \\ \chi_{ozx} & \chi_{ozy} & \chi_{ozz} \end{pmatrix} \begin{pmatrix} E_{ox} \\ E_{oy} \\ E_{oz} \end{pmatrix} \qquad (3.12)$$

The physical significance of the tensor can be seen by considering, as examples, the elements in the second row. The diagonal element χ_{oyy} determines the magnitude of the *y* component of the induced molecular dipole moment which arises from the y component of the oscillating electrical field. The off-diagonal element χ_{oyy} determines the contribution to *y* component of the dipole caused by the *x* component of the electric field, while χ_{oyz} determines the contribution to the *y* component of the dipole moment arising from the *z* component of the electrical field.

To visualize the equilibrium molecular susceptibility χ_0, we can draw arrows from common origins which have lengths proportional to the value of χ_0 in that particular

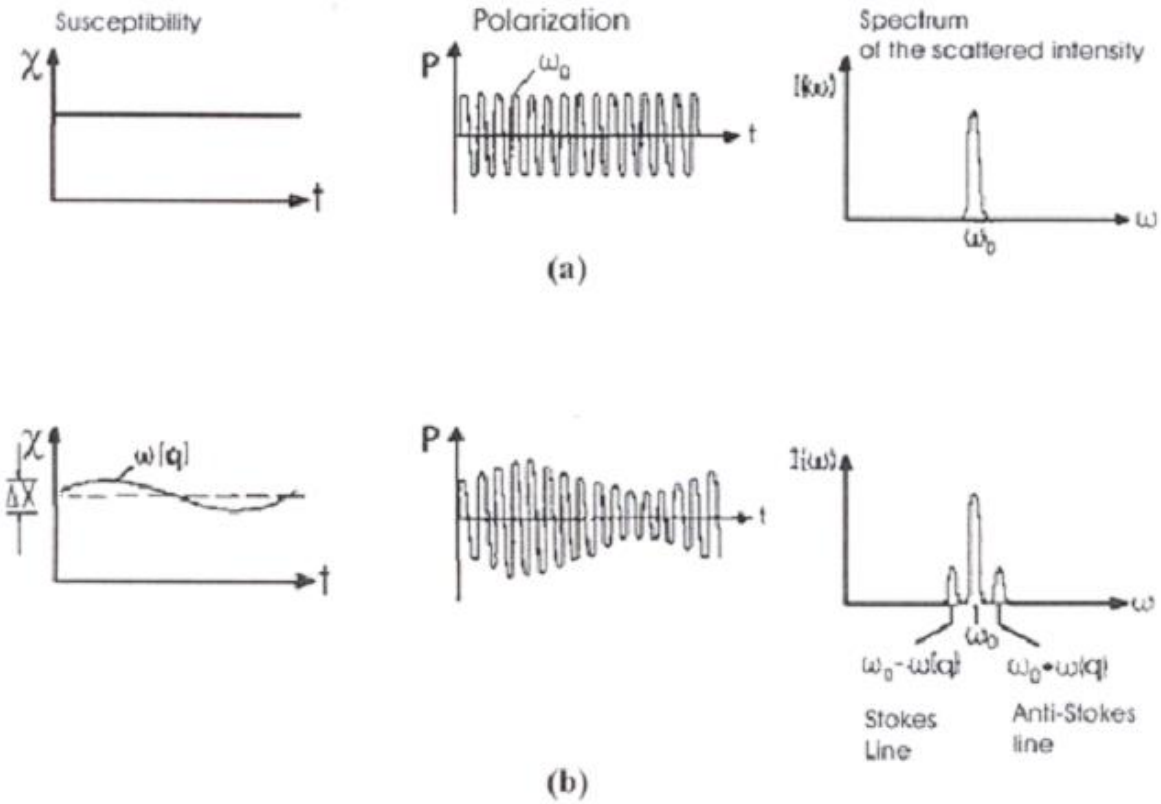

Fig 3.6 Schematic representations of the mechanics of (a) elastic and inelastic (b) light scattering (Raman scattering): (a) if the electronic susceptibility is assumed to be constant in time, the polarization ***P*** oscillates with the frequency ω_o of the incident light and, in turn, radiates only at this frequency (elastic process).

(b) If the susceptibility itself oscillates with the frequency ω (***q***) of an elementary excitation (e.g. phonon), then the oscillation of the polarization induced by the primary radiation (frequency ω_o) is modulated with frequency ω(***q***). This modulated oscillation of the polarization leads to contributions in the scattered light from the so-called Raman side bands of frequencies $\omega_o \pm \omega$ (***q***).

direction. The heads of all of these arrows will define an ellipsoid. For some purpose it is more convenient to make the length of the arrows proportional to $\sqrt{\chi_0}$ or to $\frac{1}{\sqrt{\chi_0}}$ we shall just use χ_0. Finally, we can make the susceptibility matrix much simpler if we orient this ellipsoid with its principal axes along the *x, y* and *z* axes of the coordinate system used to describe the susceptibility χ_0. In this case only the elements along the principal diagonal of χ_0, χ_{azz}, χ_{oyy} and χ_{azz} differ from zero. Fig 3.7 illustrates the susceptibility ellipsoids for two tetrahedral molecules all down to the same scale. The state of polarization of the Raman scattering yields valuable information concerning the molecular vibrations. If unpolarized light is used to excite a Raman spectrum, the scattering at 90º to the incident light will be found to be at least partially polarized. The extent of the polarization depends upon the way in which the polarizability ellipsoid varies during the vibration, so polarization measurements provide additional information about the nature of the vibration.

The molecular vibration in Fig 3.8 is taken to be a totally symmetric one. Experimentally, it is more convenient to use polarized incident light excite the spectra. Let us consider the arrangement illustrated in Fig 3.8. The exciting light is directed along the *x* axis, and the scattering is viewed at a right angle to it along the *y* axis. The polarizability ellipsoid periodically expands and contracts, that is, only the diagonal elements are changing. The induced dipole will oscillate parallel to the inducing field direction. The sample is illuminated first with light polarized in the *xz* plane (see in Fig 3.8(a)). The induced dipole oscillates in the *xz* plane, and plane polarized light is scattered in the *y* direction. Next the sample is illuminated with light polarized in the *xy* plane Fig 3.8(a). Now no light is scattered in the *y* direction because a dipole does not radiate along its line of action. The ratio of this scattered light intensity to the first is the depolarization ratio, ρ, and for this case it is zero. For molecules which have polarizability ellipsoids which are not spheres, the light scattered in the *y* direction in Fig 3.8(b) will not vanish completely if all of the different orientations of the molecule in a liquid or solution are considered, but the scattered intensities in the two experiments will still differ ($\rho < 6/7$).

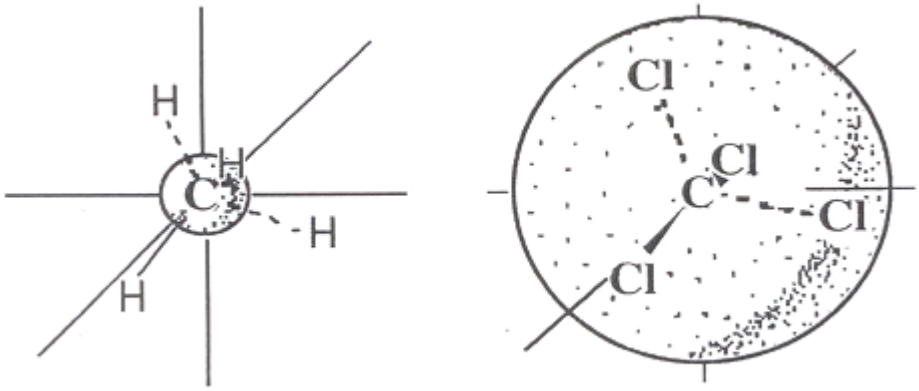

Fig 3.7 Polarizability ellipsoids for CH_4 and CCl_4 molecules

For a vibration which destroys some of the symmetry of the molecule, the intensity of the light scattered is almost the same in the two experiments (ρ =6/7). This situation is illustrated in Fig 3.8(b). Now the average value of the diagonal elements remains constant, while the off diagonal elements of the polarizability are changing; and these leads to rotation of the induced dipole away from the direction of the inducing field. Experimental determination of the depolarization ratio can usually provide a means of distinguishing symmetric from non-totally symmetric vibrations of the molecule.

3.4 Vibrational Characters of T_d Molecules

The structure assumed for the phosphate molecule is that of a regular tetrahedron where the atoms being situated at its corners. Free phosphate ion (PO_4^-) of Fig 3.9 has Tetrahedral, T_d (E identity, C_3 three-fold rotation, C_2 two-fold rotation, S_4 four-fold inversion and σ_d reflection) symmetry. The behaviour of the motion of PO_4^- with respect to symmetry operations is given in Table 3.1.

Table 3.1 The character table for T_d point group

T_d	E	$8C_3$	$3C_2$	$6S_4$	$6\sigma_d$	
A_1	1	1	1	1	1	
A_2	1	1	1	-1	-1	
E	2	-1	2	0	0	
F_1	3	0	-1	1	-1	R_x,R_y,R_z
F_2	3	0	-1	-1	1	T_x,T_y,T_z

The procedure begins by deciding on the symmetry species of the irreducible representations spanned by 3N displacements of the atoms, using the character table of the molecular point group. We find these characters by counting *1* if the displacement is unchanged under the symmetry operation, *-1* if it is changed sign,

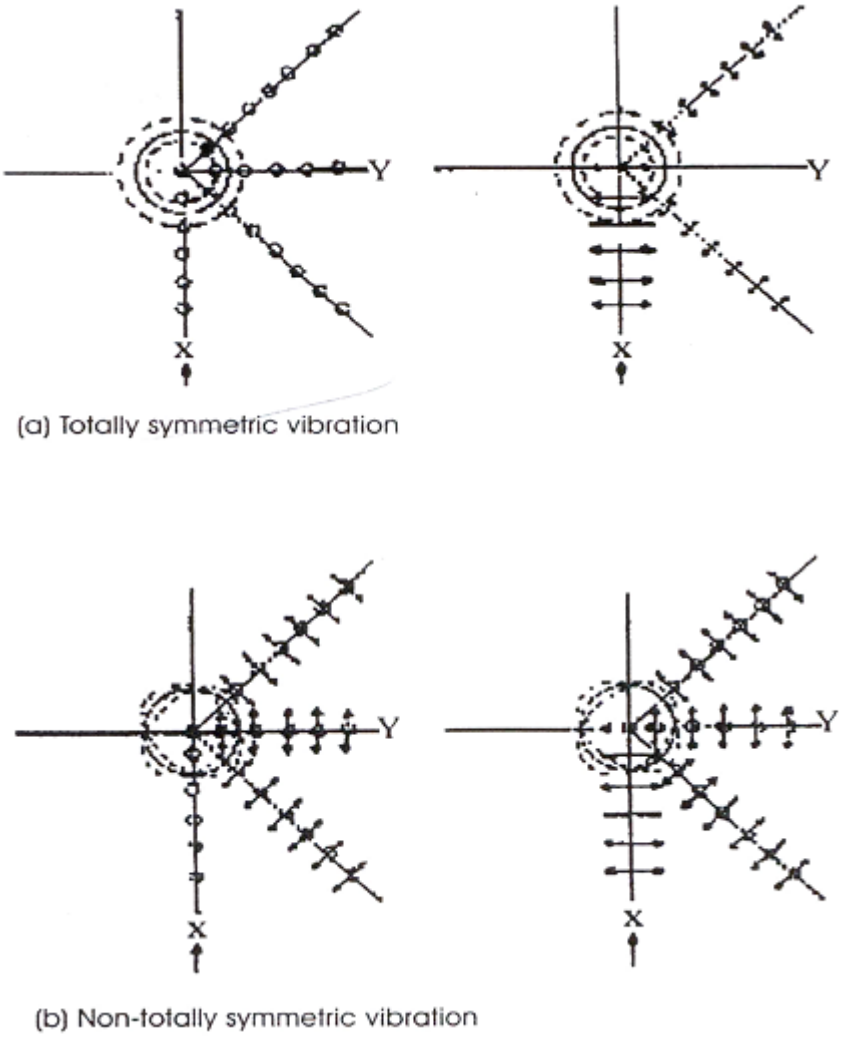

Fig 3.8 State of polarization of the Raman scattering from totally symmetric and non-totally symmetric vibrations. Arrows indicate polarization in the plane of the paper, and circles indicate polarization normal to the plane of the paper

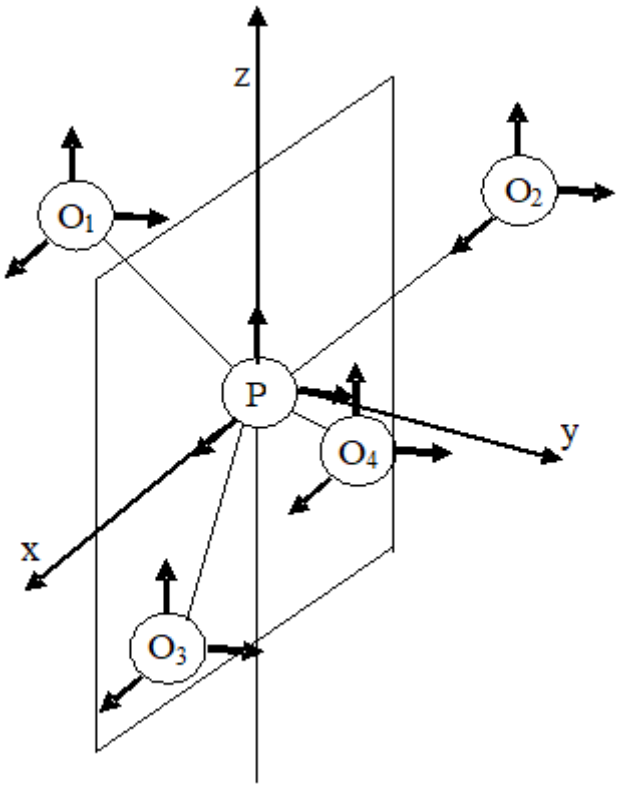

Fig 3.9 The atomic displacements of PO_4^- and the symmetry elements used to calculate the characters

and 0 if it is changed into some other displacement. Next, we subtract the symmetry species of the translations. Finally, we subtract the species of the rotation, which are also given in the characters table. There are 3 x N = 15 modes of motion, of which 3 x 5 - 6 = 9 are vibrations. The sum of the diagonals of a transformation matrix is known as the character of transformation matrix, such a table summarizing symmetry behavior is known as the character table for the symmetry point group T_d. Although the transformations matrices deal with so far do from representations of the group, they do not form the only representations. There are in fact, an infinite number of matrix representations.

A particular important one for a given crystal can be found by assigning a set of the three Cartesian displacement vectors to each atom in the crystal. Now we examine the change in these vectors upon successive application of all the symmetry elements of the group, write the general transformation matrix for each operation, and then determine the trace or character of matrix.

Under E no displacement coordinates are left unchanged and so the character $\chi(E)$ is

$$\chi(E) = 1+1+1+1+1+1+1+1+1+1+1+1+1+1+1 = 15. \quad (3.13)$$

Under C_3, no displacements are left unchanged, and so the character $\chi(C_3)$ is

$$\chi(C_3) = 0+0+0+ \text{.....} = 0. \quad (3.14)$$

Under C_2 rotation, the z-displacement of the central atom is left unchanged, why x and y components both change sign. Therefore, the character $\chi(C_2)$ is

$$\chi(C_2) = -1-1+1+0+0+ \text{.....} = -1. \quad (3.15)$$

Under S_4, the z-displacement of the central atom is reversed, the character $\chi(S_4)$ is

$$\chi(S_4) = 0+0+0+ \text{.....}+(-1) = -1. \quad (3.16)$$

Under σ_d, the z-displacement of S, O_3 and O_4 are left unchanged, 3 of the O displacements are left unchanged and three are reversed, here $\chi(\sigma_d)$ is

$\chi(\sigma_d) = 3+3-3 = 3$ (3.17)

Therefore, the sums of the diagonal elements of the complete transformation matrices give the character of the representation matrix. See also Table 3.2.

Table 3.2

	E	$8C_3$	$3C_2$	$6S_4$	$6\sigma_d$
$\chi_j(R)$	15	0	-1	-1	3

From this table, it can be shown that representations of small dimension, such as those involving one-by-one matrices; could be built up to give any number of representations involving matrices of larger dimension of much important is the process by which matrix representation is broken down into representations which consist of matrices with as small a dimension as possible. Representations that can be so broken down are said to be reducible representations and those that involve whose dimensions cannot be further decreased are said to be irreducible representations. In the molecular problem, the distributions of the vibrations among the irreducible representations of the point group can be calculated by the "*magic formula*",

$$n^{(\gamma)} = \frac{1}{h}\sum_j h_j \chi_j^{(\gamma)*} \chi_j \qquad (3.18)$$

where $n^{(\gamma)}$ is the number of vibrations of species γ, h is the order of group or the number of symmetry operations in the group, h_j is the number of symmetry operations in the j^{th} class, $\chi_j^{(\gamma)*}$ is the character of irreducible representation and χ_j is the character of reducible representation (from the character table).

For T_d point group,

$n_{tot}^{A_1} = [1x1x15 + 8x1x0 + 3x1x(-1) +6x1x(-1) + 6x1x3] = 1$

$n_{tot}^{A_2} = [1x1x15 + 8x1x0 + 3x1x(-1) +6x(-1)x(-1) + 6x(-1)x3] = 0$

$n_{tot}^{E} = [1x2x15 + 8x(-1)x0+3x2x(-1) +6x0x(-1) + 6x0x3] = 1$

$n_{tot}^{F_1} = [1x3x15 + 8x0x0 + 3x(-1)x(-1) + 6x1x(-1) + 6x(-1)x3] = 1$

$n_{tot}^{F_2} = [1x3x15 + 8x0x0 + 3x(-1)x(-1) + 6x(-1)x(-1) + 6x1x3] = 3$

and thus, $n_{tot} = A_1 + E + F_1 + 3F_1$ (3.19)

The representation n_{tot} includes all motions of the crystal. Since the interest at this is only in the vibrational motion we can separate out and discard the contribution due to translation and rotation. If the assigned translations and rotations, indicated in the last column of the Table 3.1, are removed one has

$$n_{vib} = n_{tot} - n_{tran} - n_{rot} = A_1 + E + 2F_2. \quad (3.20)$$

Fig 3.10 shows the normal vibrations of a tetrahedral molecule. If the symmetry species of a normal mode is the same as any of the symmetry species of x, y, or z, mode is infrared active. Refer to the T_d character table to establish the symmetry species of x, y, and z; it is F_2. The symmetry species of the *normal modes* are $A_1 + E + 2F_2$. Therefore, only the F_2 modes are *infrared active*. The distortions accompanying the F_2 mode is the same as the symmetry species of a *quadratic form,* the mode is *Raman active*. The *quadratic forms* span $E + F_2$, normal modes which are *Raman active*. The A_1 mode, which is *inactive*, is the symmetrical *"breathing"* mode of the molecule. A_1 breathing mode is neither infrared nor Raman active.

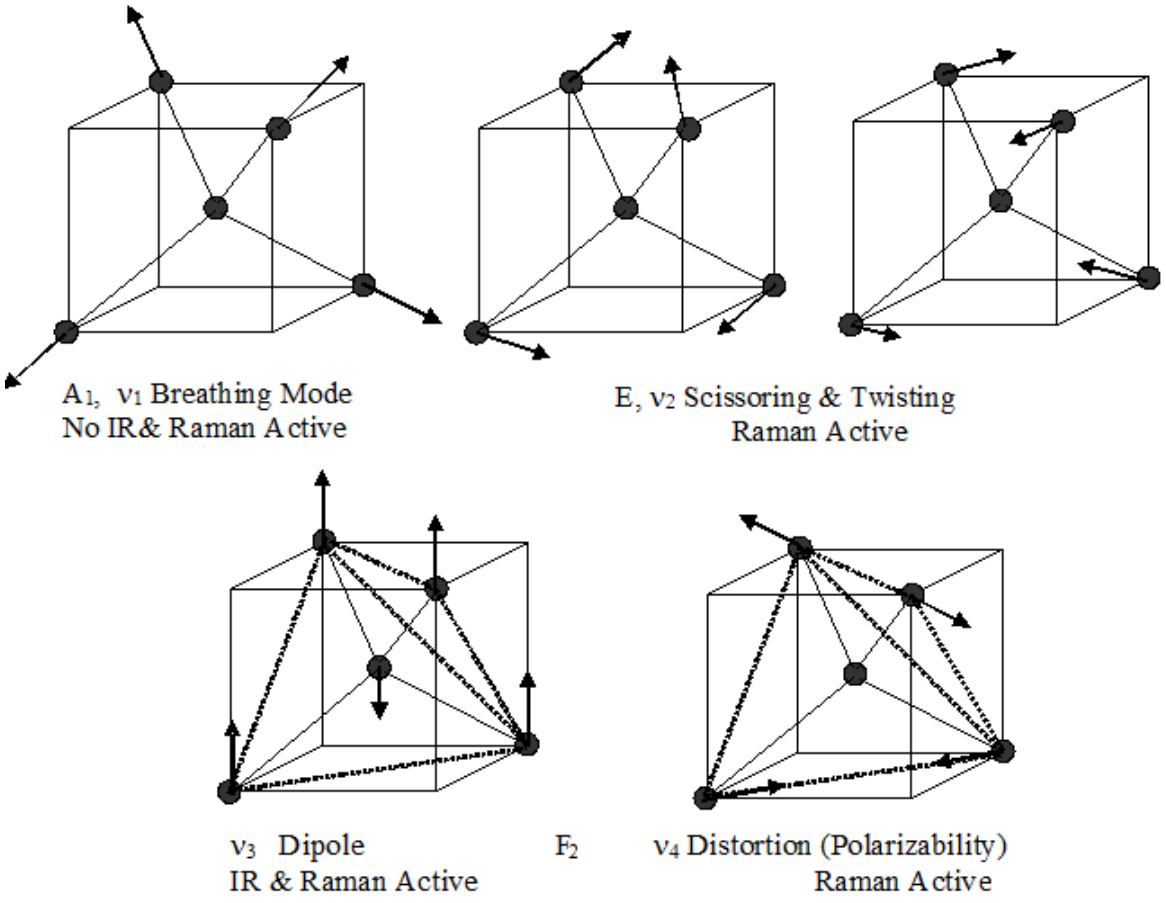

Fig 3.10 Normal vibrations of a tetrahedral molecule

3.5 Optical Set-Up of Raman Spectrometer

The patented InPhotonic fiber optic Raman probe utilizes micro-optic components for delivering for laser excitation source to the sample and for collection of scattered light resulting in a compact probe head that is fiber optically coupled to the laser source and spectrograph.

Through the efficient use of bandpass, dichroic and edge filters for separating the excitation and scattered light, the InPhotonics probe utilizes a back scattering (θ=180º) sampling geometry. The Raman probe backscattering collection geometry allows easy sample alignment and provides optimum throughput because of the totally overlap between the excitation and collections cones. The schematic diagram of the internal optics of the Raman probe is shown in Fig 3.11. The InPhotonics Raman probe also incorporates laser safety features such as the beam attenuator/cover and the LED emission indicator. The LED emission indicator at the probe had can be configured by the user so that when the laser source is turned on the LED lights up indicating that laser radiation is emitted from the probe aperture. The LED emission indicator is also visible through laser safety glasses. The InPhotonics Raman Probe is coupled to the excitation source and the spectrograph via two optical fibers to allow remote measurements of samples. Each Fiber optic subunit is provided in a projective jacket. A specially designed fiber optic cable was built for the Raman probe that provides both protection to the optical fibers and also integrates electrical wires necessary to power up the probe LED safety. The fiber optic subunits and two 20-gauge hookup wires for the LED indicator are then woven together and encased in an external protective jacket. The jacketing material is a stainless-steel interlocking cable. The resulting cable has a diameter of nearly 0.25 inches and remains fairly flexible.

The excitation light source was the solid-state diode laser (green laser) with the constant output 500 mW at 532 nm. In order to avoid the local heating of sample, and incident power at the sample was usually adjusted to be 30-40 mW. The spot size of the laser varies with the transmission properties of the sample under measurement. Using a collection fiber that is twice the size of the excitation fiber

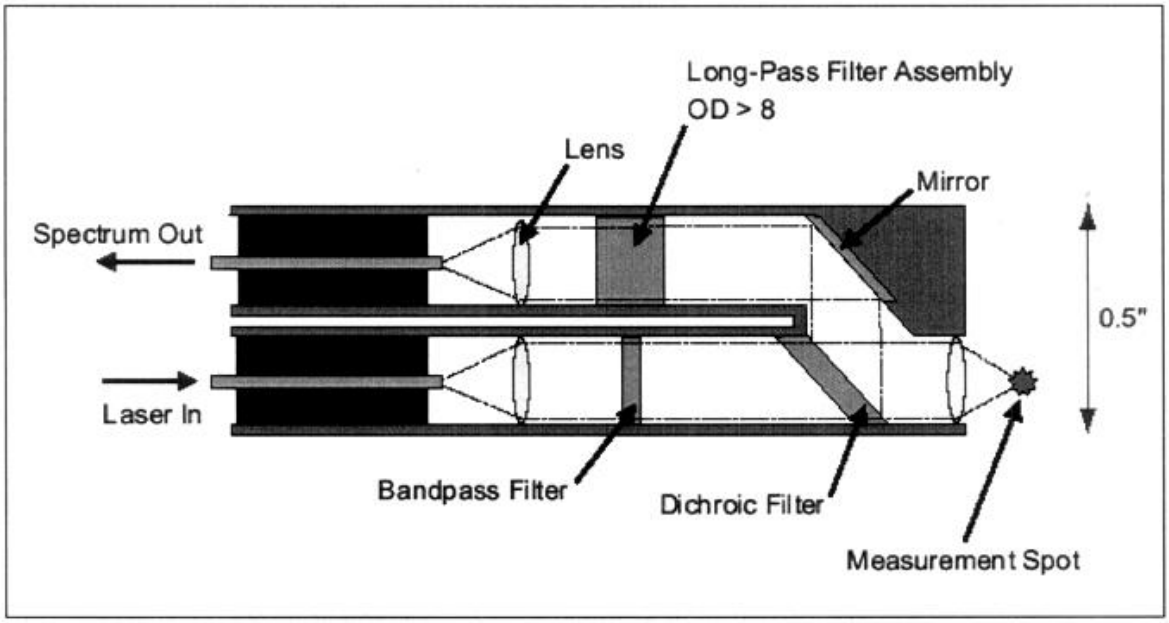

Fig 3.11 Schematic representation of the Raman Probe

ensures maximum signal collection of transparent as well as opaque materials.

3.6 Optical System of FTIR Spectrometer

An FTIR uses one of several optical systems; the Perkin-Elmer 600 FTIR spectrometer relies a Michelson Interferometer with the New Ceramic Light Source, which is electrically heated, is shown in Fig 3.12. After passing through the aperture, light is turned into a parallel by the collimator mirror and enters the beam splitter. A germanium film, deposited on a potassium bromide substrate via evaporation, comprises the beam splitter; it splits the single beam into two, reflecting one to the fixed mirror and transmitting the other to the moving mirror. Both mirrors reflect their beams back to the beam splitter; part of each returning beam is reflected and transmitted. The transmitted light from the fixed mirror and the reflected light from the mirror recombine and interfere with each other as they travel towards the collecting mirror interference is either constructive or destructive. From the collecting mirror, the parallel infrared beam creates an image of the light source in the center of the sample compartment. Collecting mirror gathers the beam that passed through the sample and reflects it to a pyroelectric detector DLATGS (L-alanine doped deuterated triglycine sulfate) as the interferogram. After reaching the detector, the interferogram undergoes several treatments before being sent to the computer. It is amplified by the preamplifier and the automatic gain amplifier, passes through high-pass and low-pass filters, and is digitized by the 20-bit A/D converter. After the signal is digitized into the interferometer memory, it travels through the SCSI interface to the PC where Hyper-IR Software transforms the interferogram into a spectrum.

The Fourier Transform (FT) process is most easily visualized in terms of the emission of radiation. The technique can also be applied to absorption. A 'white' source would show a single decay signal with no beats; an approximation to this is shown in Fig 3.13(a), where a very broad emission line (which can be considered as a white source covering a limited region of the spectrum) and its Fourier transform are shown. Although the time domain signal decays very rapidly, it does

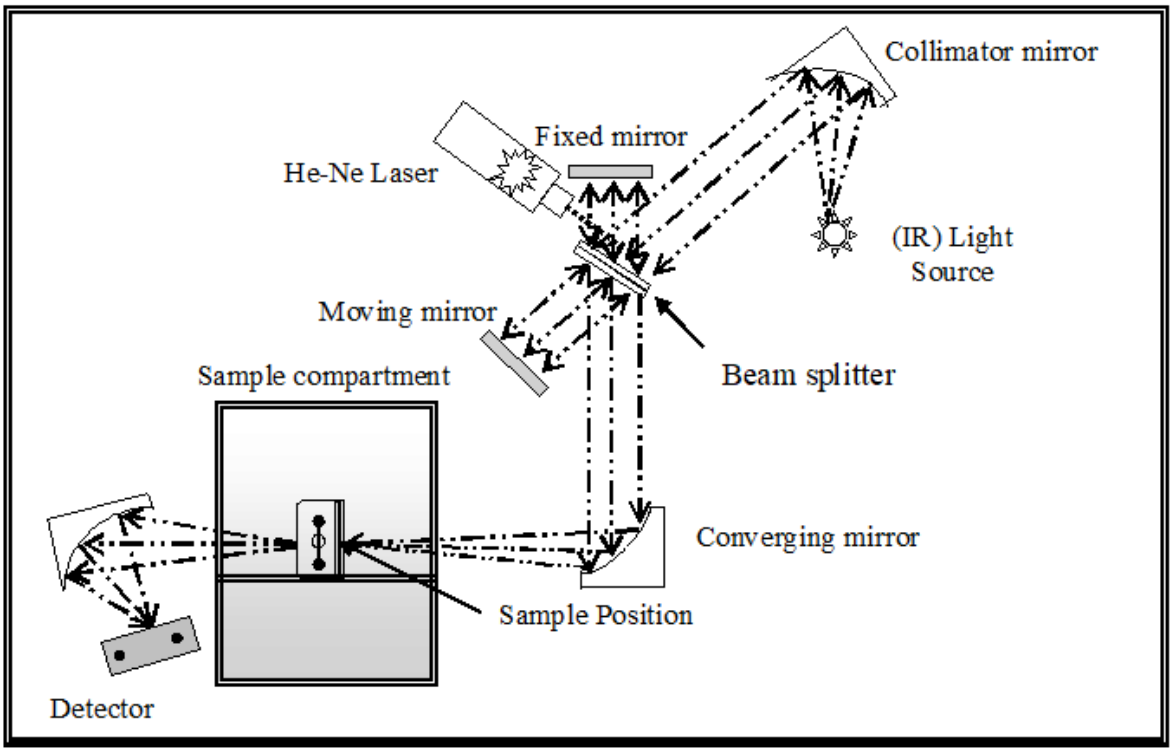

Fig 3.12 Schematic diagram of the FTIR system

show some beats; this is because the broad emission line is only an approximation to a proper white source.

We can now imagine an absorbing sample making some 'holes' in this radiation, as shown on the left-hand side of Fig 3.13(b), with its resulting FT signal on the right. Although we may find it difficult to imagine Fourier- transforming (or even just adding up) the absence of radiation at some frequencies, in practice a detector will collect a perfectly sensible signal which can be stored by a computer, transformed, and displayed as the normal absorption spectrum.

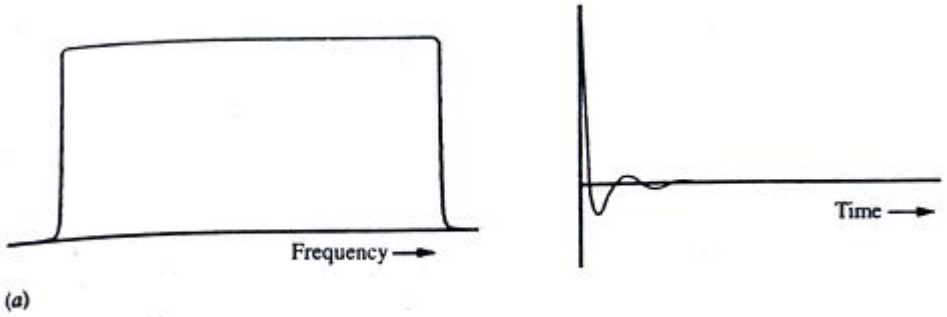

Fig 3.13 (a) An approximation to a 'white' source and its Fourier transform

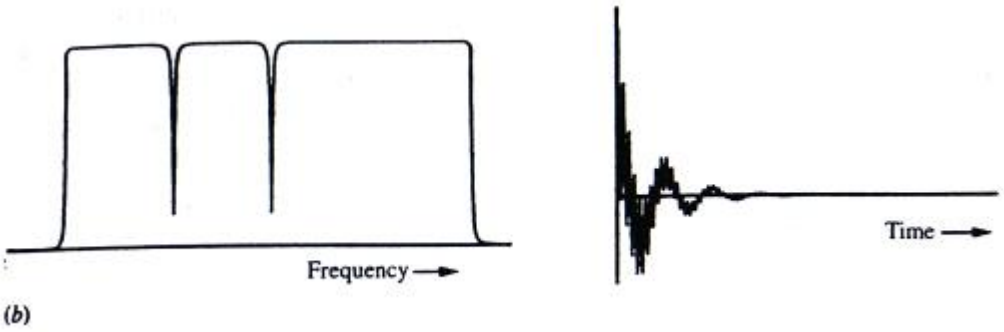

Fig 3.13(b) Some absorptions from a 'white' source and their Fourier transform

CHAPTER IV

EXPERIMENTAL SET-UP AND MEASUREMENT

The crystal growth, the sample preparation, the measurements of temperature dependent ionic conductivity and light-induced photoconductivity of the Zinc Ammonium Phosphate, ZnNH4PO4 [ZAP] form the essential part in the present experimental work. Some details will be described because they are important in practice based on doing experiment in this work and also in the related fields [1, 2, 3, 8, 11, 19, 20, 21].

4.1 Growth of $ZnNH_4PO_4$ [ZAP] Single Crystal

Most of the ionic crystals can easily be grown from their aqueous solutions. Single crystals of Zinc Ammonium Phosphate, $ZnNH_4PO_4$ [ZAP] were grown by the slow evaporation method from aqueous solutions containing the aqueous equimolar ratio of Zinc Sulphate, $ZnSO_4$ and Ammonium Dihydrogen Phosphate, $NH_4H_2PO_4$ [ADP]at room temperature (30 °C). Laboratory grade of those salt powders and distilled-water were used to growth for single crystals.

The supersaturated solution is filtered into the beaker and warmed about 5°C higher than the previous temperature. The beaker is then covered with very thin plastic and set aside at 30°C for a few days. There are five seed crystals drawn at the bottom of the beaker after seven days. Seed crystals of complete morphology (shape and size) and quality (homogeneous and transparent) were withdrawn with tweezers and placed on filter paper to dry for one hour. At room temperature, those crystals are colourless. Photograph showing the as-grown crystal of ZAP is shown in Fig 4.1.

4.2 Structural Analysis by Powder XRD Measurement

Qualitative analysis on powder samples of the single crystal of ZAP at room temperature was investigated by computer-controlled RIGAKU MULTIFLEX X-ray diffractometer *using* Ni-filter with CuK_α radiation, λ = 1.54056 Å and $10° < 2\theta < 70°$ with the scan step size of 4°.

Fig 4.1 Photograph showing the as-grown crystal of $ZnNH_4PO_4$ [ZAP]

RIGAKU MULTIFLEX X-Ray Diffractometer system

The operation conditions of the x-rays diffractometer using copper target has the tube voltage (40 kV) and the tube current (20 mA) for the whole operation. X-rays radiated from the x-ray tube with copper target is rest retained by divergence slit (DS) and hit the sample placed in the center of goniometer. The x-ray diffracted beam form the specimen is focused on the receiving slit (RS) placed in the position opposite to the x-ray focus in relation to the sample. The diffracted x-ray is received by an x-ray detector such as NaI(Tl) scintillation counter and converted to electric signals, and then recorded by PC with the counting rate (counts per second or percentage). The block diagram of the XRD system is shown in Fig 4.2.

The collected data were used to refine the unit cell parameters from the observed 2θ values with JCPDS (Joint Committee on Powder Diffraction Standards). In the recorded XRD pattern, all the peak positions are in good agreement with JCPDS (Joint Committee on Powder Diffraciton Standards) file data for those crystalline powders. In the JCPDS x-ray powder data fills the diffraction pattern of the material is identical by the interplanar spacing *d*, corresponding to each diffraction line and the relative intensity of the diffracted X-ray.

4. 3 FTIR Measurement

There are in general several types of motion that a molecule may undergo. *First,* the molecule as a whole may move through space in some arbitrary direction and with a particular velocity. This type of motion is called *translational motion* and with it we associate the translational motion of the molecule. *Second,* the molecule may rotate about some internal axis. Again, any such axis may be resolved into components along the x, y, and z axes of a Cartesian coordinate system, so that any rotation of the molecule may be resolved into three mutually perpendicular components. Finally, the molecule may vibrate. Each of the vibrational motions of a molecule occurs with a certain frequency, which is characteristic of the molecule and of the particular vibration. The frequency of light required to cause a transition for a particular vibration is equal to the frequency of that vibration, so that we may measure the vibrational frequencies by measuring the frequencies of light which are

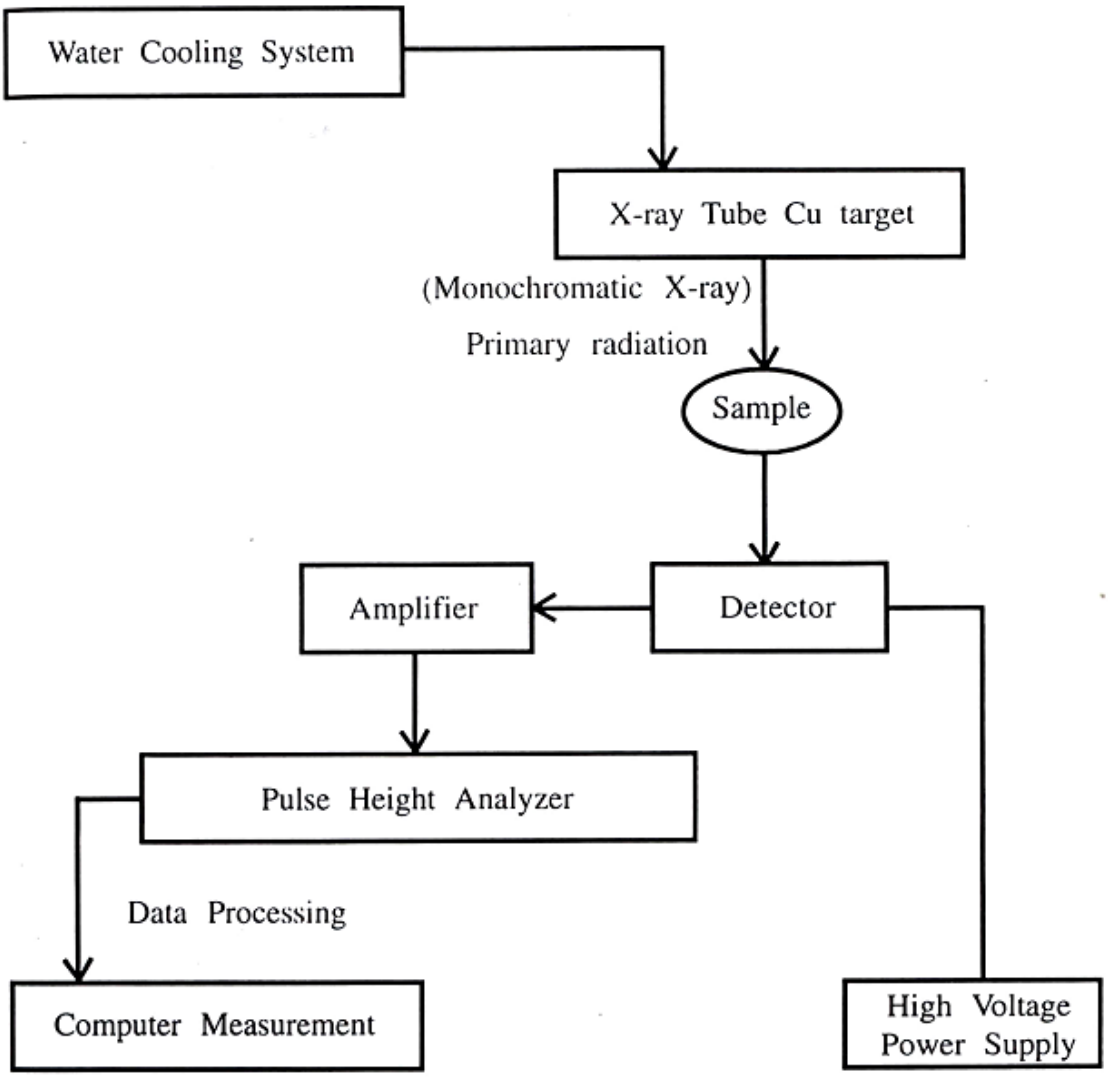

Fig 4.2 Block diagram of X-rays diffractometer system

absorbed by the molecule. As it happens, light of this wavelength lies in the so-called infrared region of the spectrum. IR spectroscopy, then, deals with transitions between vibrational energy levels in molecules, and is therefore also called vibrational spectroscopy. An IR spectrum is generally displayed as a plot of the energy of the infrared radiation versus the percent of light transmitted by the compound.

Potassium Bromide (KBr) pellets are used to obtain the infrared spectra of solids, and are particularly well suited to powder samples. KBr is an inert, infrared transparent material, and acts as a support and a diluent for the sample. Moreover, the material must be transparent to the incident to the incident IR radiation and therefore alkali halides are normally used in transmission methods. The most commonly used alkali halide is potassium bromide (KBr), which is completely transparent in the middle IR region.

In the present work, IR transmission spectrum of $ZnNH_4PO_4$ [ZAP] single crystal with the ratio of (1 : 100 wt%) Potassium Bromide, KBr have been recorded on Perkin Elmer FTIR Spectrometer at room temperature. The photograph of the FTIR system is shown in Fig 4.3. The experimental conditions were used as follow:

Measurement mode : %T
Wavenumber range : 400 cm^{-1} – 4000 cm^{-1}
Measuring time : 60 s
Apodization function : Happ-Genzel
Resolution : 4 cm^{-1}
Method : KBr disc.

Fig 4.3 Photograph of the FTIR spectrometer

4.4 Raman Scattering Measurement

Raman spectra can be observed when the monochromatic (laser) light is scattered by molecules in solids, liquids, or gases. The energy of the light used should not correspond to an allowed electronic or vibrational transition, that is, it should not be resonantly absorbed by the molecules. Since it is the scattered light which is of interest and this will be very low in intensity compared to the initial intensity of the light source.

The present investigation was carried out to the study of molecular vibrations of phosphate molecules in ZAP crystal by the use of RSI-2001S Raman spectrometer. Photograph showing the experimental setup of Raman scattering system is shown in Fig 4.4. The measurement conditions for Raman scattering experiment have been employed as the followings:

Crystal holder	: Black coated copper cylindrical block with the dimension (3 cm in outer diameter x 2.54 cm in inner diameter x 5 cm in height)
Laser source	: Solid-state diode laser
Colour	: Green
Wavelength	: 532 nm
Scattering geometry	: 180° back-scattering
Integration time	: 20 s.

4.5 Thermogravimetric (TGA) and Differential Thermal Analysis (DTA) Measurement

The Differential Thermal Analysis (DTA) measurement with higher accuracy was carried out along with Thermo-Gravimetric Analysis (TGA) using the (Perkin Elmer) Pyris Diamond DTG Analyzer as shown in Fig 4.5(a) and Fig 4.5(b). In the present work, 5.888 mg weight powdered crystal sample of ZAP was used for measurement. Aluminium (Al) pan was used as the standard sample. TGA-DTA measurements were done under the experimental conditions.

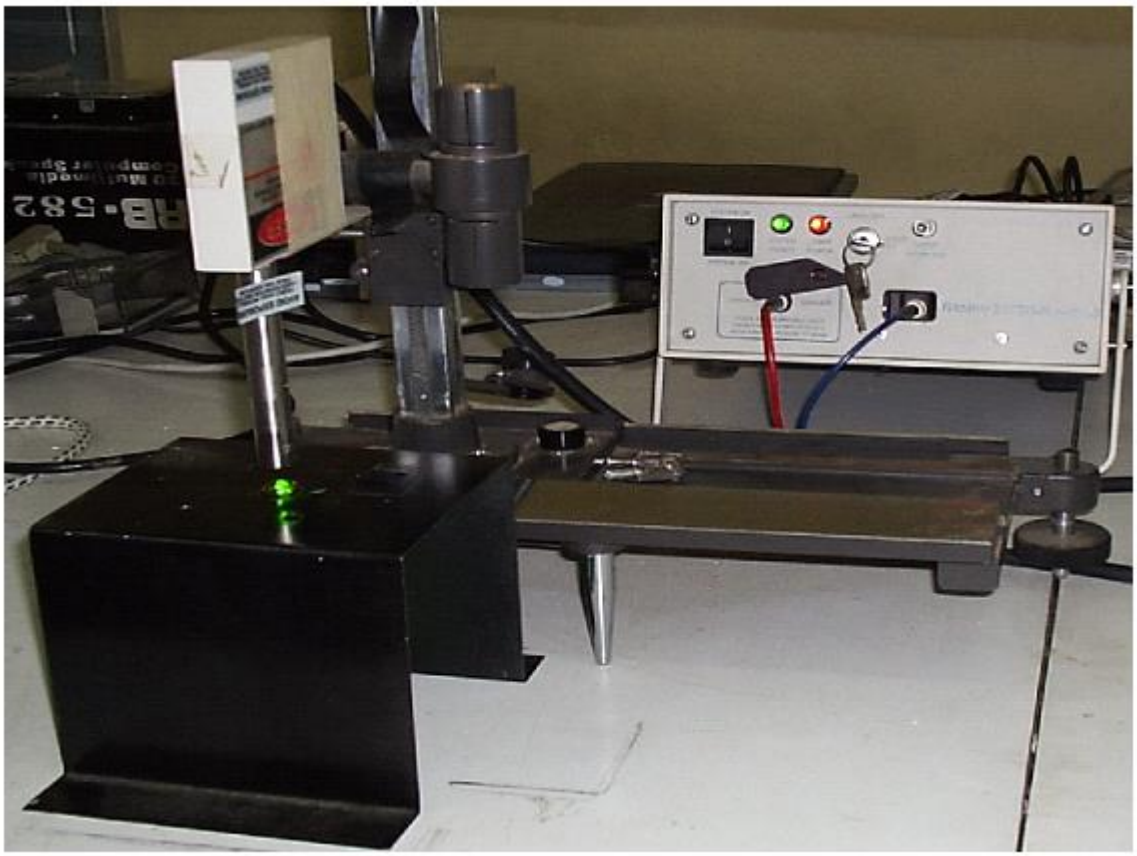

Fig 4.4 Photograph showing the experimental setup of RSI-2001S Raman spectrometer

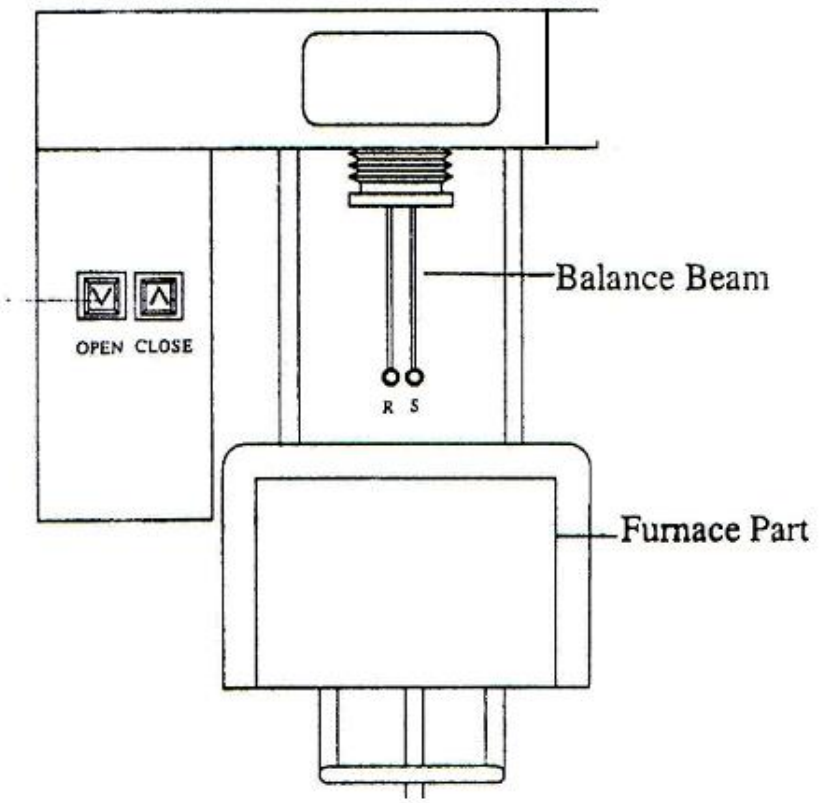

Fig 4.5(a) Thermo-balance of (Perkin Elmer) Pyris Diamond DTG Analyzer

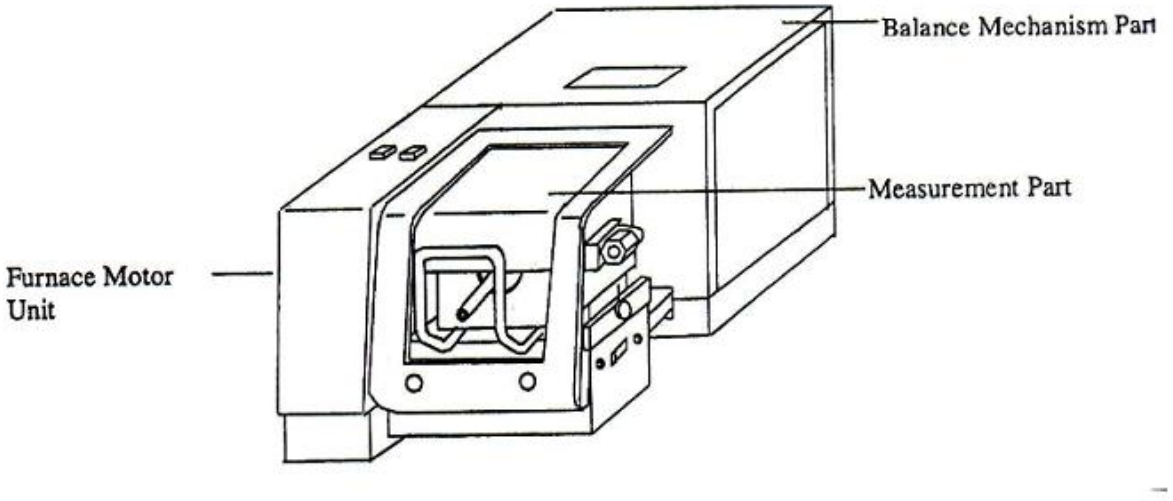

Fig 4.5(b) (Perkin Elmer) Pyris Diamond DTG Analyzer module (instrument)

Sample weight	-	5.888 mg
Pan	-	Al
Atmosphere	-	N_2
Flow Rate	-	50 [ml/min]
Start Temperature	-	30 °C
End Temperature	-	550 °C
Heating Rate	-	20 °C/min

4.6 Sample Preparation for Thermal and Light-Dependent Electrical Conductivity Measurements

Of course, an as-grown single or mixed crystal contains two or more single crystals with the various/multi crystal domains. These domains can be viewed as the different in optical media (for example, gray, transparent, white, etc..) under the crossed-polarizer. Thus, crystals with single domains, i.e. to get a single crystal of ZAP, were cut (0.80 x 0.62 x 0.31 cm^3 for temperature-dependent conductivity measurement) and (0.94 x 0.82 x 0.36 cm^3 for light-dependent conductivity measurement) by nylon throat and polished with the wet filter papers.

Hence, the crystal was fixed on glass plate and silver contacts were made over the cross-sectional area (for temperature-dependent conductivity measurement) and side-wall (for light-dependent conductivity measurement) of the sample to ensure good electrical continuity. The sample was, then sandwiched between two copper electrodes (plates) as the above conditions. Finally, the sample was placed in the sample holder that was surrounded by black-coated plastics (for light-dependent conductivity measurement) and also the sample was then sandwiched between two copper plates, which placed in the steel housing chamber (for temperature-dependent conductivity measurement).

4.7 Temperature Dependent Electrical Conductivity and Dielectric Measurements

The sample was sandwiched between two thin copper plates to ensure a good electrode contact. The crystal was placed in the sample holder two thick copper plates with the dimensions of 4.5 cm and 1.2 cm in diameters with 0.5 cm and 0.2 cm in height/thick. The crystal holder then was inserted into the steel housing/chamber that surrounded by asbestos to prevent the heat loss.

The photograph of ionic conductivity measuring unit with temperature control system is shown in Fig 4.6. Sample holder is immersed in the heating copper chamber. Mica sheets are used between crystal and chamber to have better thermal conductivity and to protect the electrical conductivity. In order to provide better electrical contact the silver paste is applied evenly on both surfaces of the crystal.

Temperature dependent ionic conductivity and capacitances of $ZnNH_4PO_4$ [ZAP] single crystal was observed in the temperature range from 30 °C to 360 °C by the use of PC-based temperature controller FOTEK MT-20 (up to 2000 °C). Temperature dependent resistances were measured by using FUKE FK-9208K multimeter (up to 2000 MΩ). The temperature sensor of K-type thermocouple (up to 800 °C) was inserted near the sample to record real temperatures throughout the measurement (see Fig 4.6). The copper block holder (heater chamber) was heated by 300W heater coil. The conductivity has been calculated using the formula $\sigma = \frac{l}{RA}$ where l is the thickness of the sample, A is the area of cross-section of the electrodes and R is the resistance.

Temperature dependent capacitances were measured by using WHDZ CM9601A Capacitance meter (2μF – 2000 pF). The value of dielectric constant ε_r or ε have been calculated by the relation given below,

$$\varepsilon_r = \frac{1}{\varepsilon_0}\frac{Ct}{A}$$

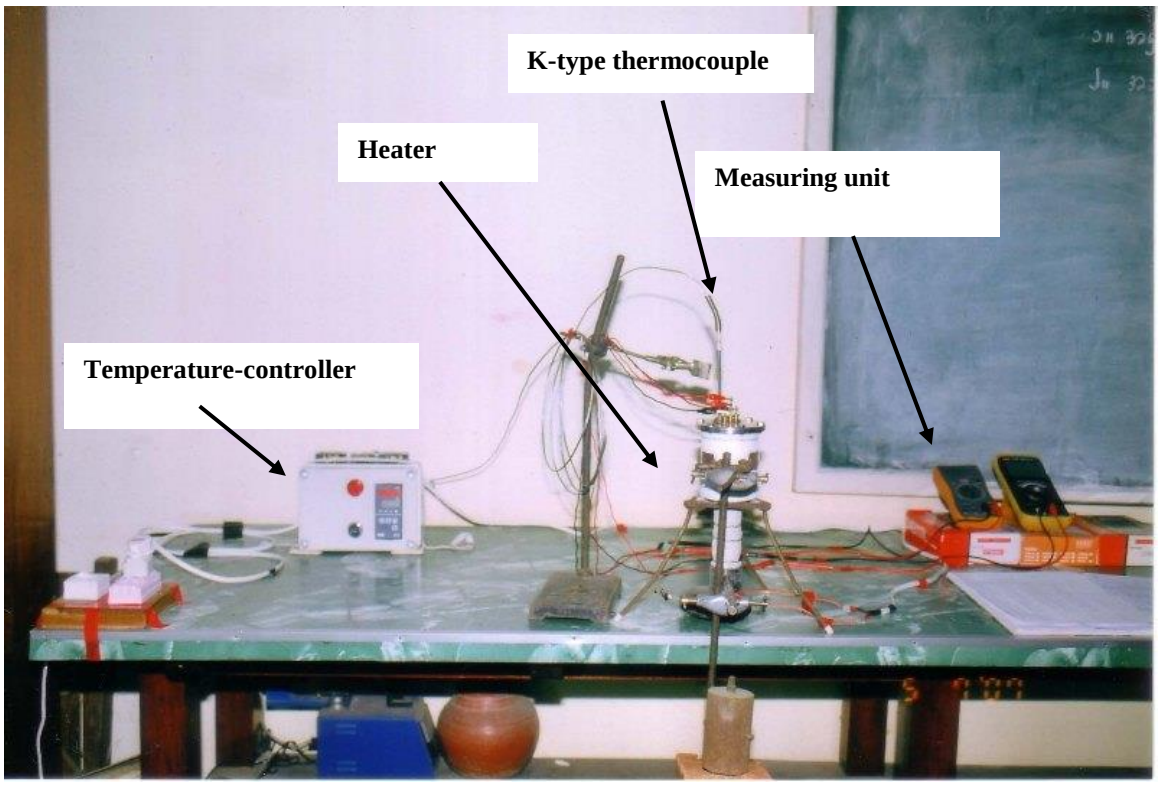

Fig 4.6 Experimental setup of temperature dependent ionic conductivity measurement

where C is the capacitance, t is the thickness of the crystal, A is the cross-sectional (surface) area of the crystal and ε_0 is the permittivity of free space ($8.854187817 \times 10^{-12}$ C^2 / Nm^2).

4.8 Light Dependent Conductivity Measurement

Light dependent electrical characterizations of ZAP single crystal have been investigated by two different electrical powers of 20W (fluorescent tube) and 100W (light bulbs) light sources to study the photo-sensitivity of the crystal. The light intensity sensor of Si-photodiode (SEW, LIGHTMETER 2330LX) was placed near the sample with parallel position to record real intensities of light sources throughout the measurement. Light dependent resistances and voltages of the crystal under increase in illuminations were measured by WHDZ DT9205M digital multi-meter. Experimental setup of photo-conductivity measurement with 20 W electrical power of light source is shown in Fig 4.7(a) and Fig 4.7(b).


20W, White
Light Source
Si Photodiode
sensor
Sample with
copper

nt

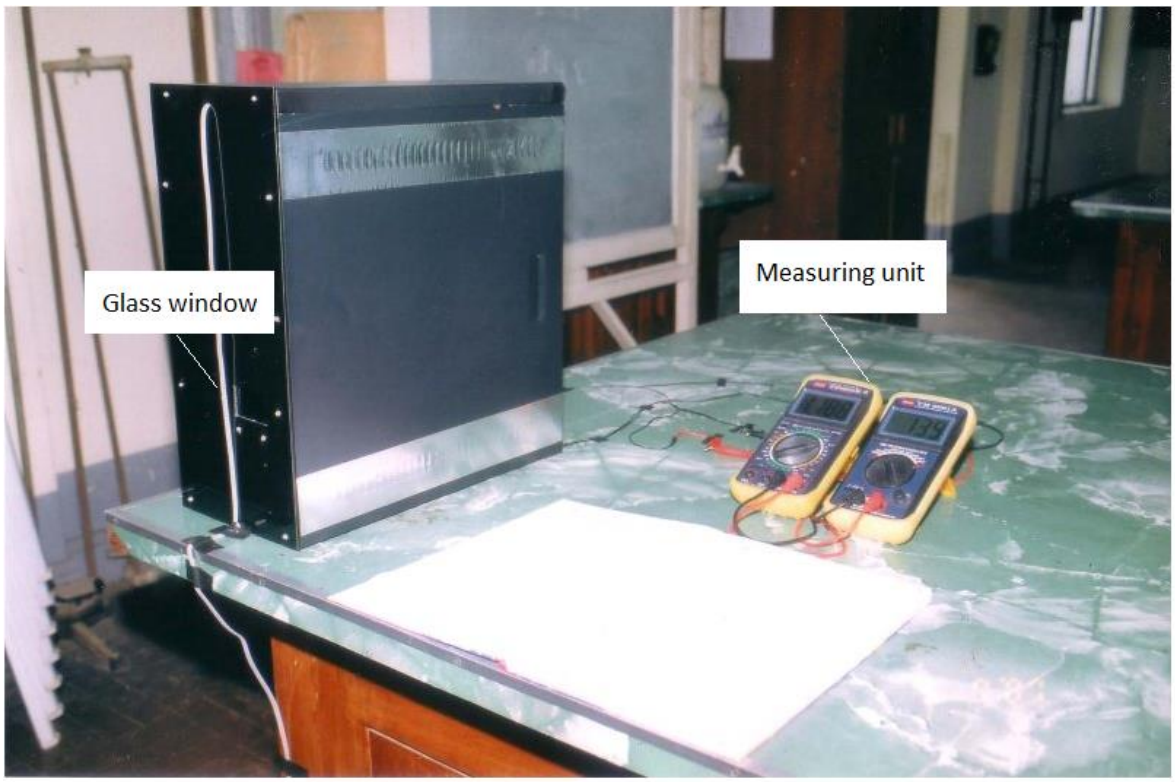

Fig 4.7 (b) External setup of photo-conductivity experiment

CHAPTER V
RESULTS AND DISCUSSION

Single crystal of $ZnNH_4PO_4$ [ZAP] is a hydrogen bonded-ionic compound that exhibits the phase change with ionic conductivity at high temperature. Above the transition point, the values of electrical conductivity enable one to classify the high temperature phases of the materials. Experimental results of some illustrations with detail explanations such as both spectral and graphical analysis are presented in this chapter.[4, 12, 20, 21]

5.1 Powder XRD Study

X-ray diffraction data were collected from powder samples of crystals using a PC-controlled RIGAKU MULTIFLEX, automated X-ray diffractometer with monochromatic CuK_α (λ = 1.54056 Å) using Ni-filter (scan speed 4°/min). The NaI(Tl) scintillation counter was used to detect the diffracted X-rays from the sample. The measurement was taken from 10 to 70° with 2θ diffraction angle. Lattice parameters were determined from the indexed data using experimental results of low angle reflections. Powder XRD patterns of $ZnNH_4PO_4$ [ZAP] crystal at room temperature are shown in Fig 5.1.

According to the powder X-ray diffraction analyses, the crystal structures of $ZnNH_4PO_4$ [ZAP] crystal analogous to orthorhombic lattice at room temperature. Experimental data of peak locations, 2θ (diffraction angles), miller indices (hkl) and atomic spacing "*d*" and intensity "I" of those crystals are presented in Table 5.1 to calculate the lattice parameters. The lattice parameters are evaluated by using crystal utility of the equations of $\frac{1}{d^2}=\frac{h^2}{a^2}+\frac{k^2}{b^2}+\frac{l^2}{c^2}=\frac{4\sin^2\theta}{\lambda^2}$. The obtained lattice parameters of ZAP are *a* = 6.00 Å, *b* = 12.57 Å and *c* = 16.12 Å respectively.

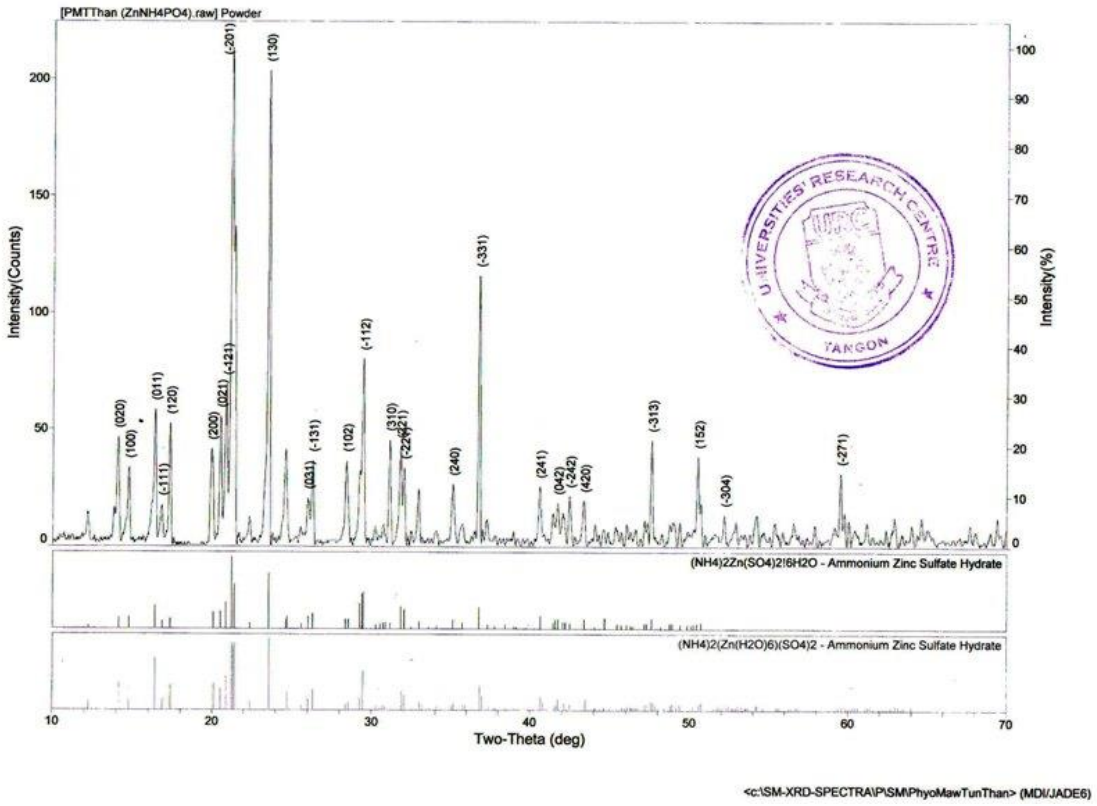

Fig 5.1 Powder XRD pattern of $ZnNH_4PO_4$ [ZAP] single crystal

Table 5.1 Powder XRD data of $ZnNH_4PO_4$ [ZAP] single crystal

Line No	2θ (degree)	d (Å)	(hkl)	I (%)
1	14.08	6.28	(020)	14.0
2	14.76	6.00	(100)	34.6
3	16.36	5.41	(110)	31.0
4	16.80	5.27	$(\bar{1}11)$	9.0
5	17.30	5.12	(021)	12.0
6	19.92	4.45	(002)	21.0

Lattice parameter a = 6.00 Å

b = 12.57 Å

c = 16.12 Å

5.2 Raman Scattering Study

Vibrational characterizations of Phosphate, PO_4^{3-} molecules (non-linear type molecules) in the ZAP single crystal were observed by Raman Spectroscopic experiment between the Raman shift range 300 cm^{-1} and 4000 cm^{-1} region at room temperature. According to vibrational analysis of a free phosphate, PO_4^{3-} or ammonium, NH_4^+ that obeys tetrahedral T_d-symmetry and it has four types of fundamental modes denoted as ν_1-symmetric-stretching, ν_2-bending (scissoring or twisting), ν_3-dipole and ν_4-polarization. These four fundamental modes of vibrations are Raman active. Also, water (non-linear) molecule has three types fundamental vibrations, namely; ν_1-mode (Asymmetric-stretching), ν_2-mode (bending) and ν_3-mode (symmetric-stretching).

Raman spectra of Zinc Ammonium Phosphate, $ZnNH_4PO_4$ [ZAP] is shown in Fig 5.2. Experimental data of ZAP crystal (Raman shifts or frequencies and corresponding vibrational mode assignments) are tabulated in Table 5.2. Four fundamental modes of phosphate, one fundamental mode of ammonium and one fundamental mode of water molecules were observed and assigned in this work.

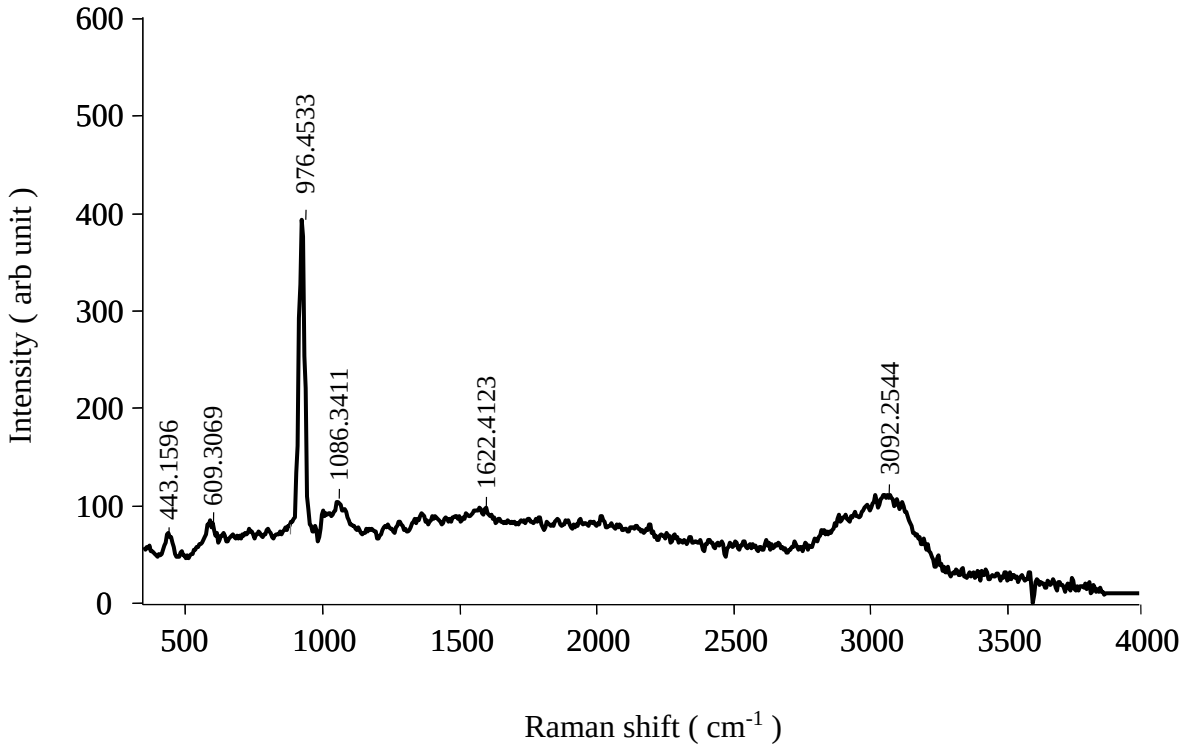

Fig 5.2 Raman spectrum of ZAP crystal at room temperature

Table 5.2 Raman shifts (frequencies) and corresponding vibrational mode assignments of phosphate, ammonium and water molecules in ZAP crystal

Line No	Raman shift (cm^{-1})	Vibrational mode assignments of molecules	Vibrational characters
1	443	$\nu_2(PO_4^{3-})$	Bending
2	609	$\nu_4(PO_4^{3-})$	Polarization
3	976	$\nu_1(PO_4^{3-})$	Symmetric-stretching
4	1086	$\nu_3(PO_4^{3-})$	Dipole
5	1622	$\nu_2(NH_4^{+})$	Bending
6	3092	$\nu_3(HOH)$	Symmetric-stretching

5.3 Fourier Transform Infrared Spectroscopic Study

An IR spectrum is generally displayed as a plot of the energy of the infrared radiation versus the percent of light transmitted by the compound. IR transmission spectrum of $ZnNH_4PO_4$ [ZAP], crystal with KBr disc method was recorded by Perkin Elmer FTIR Spectrometer within the wavenumbers of 400 cm^{-1} - 4000 cm^{-1} region at room temperature as shown in Fig 5.3. Recorded wavenumbers and corresponding vibrational mode assignments of $ZnNH_4PO_4$ [ZAP] crystal are tabulated in Table 5.3.

According to vibrational analysis of a free phosphate molecule, it has four types of fundamental modes of vibrations. In the recorded FTIR spectrum, only three fundamental modes of phosphate and three fundamental modes of water molecules are observed and assigned. The ν_2-mode (bending) of phosphate was not found in this FTIR spectrum. Normally, this mode is appeared within the wavenumber region of 400 cm^{-1} – 430 cm^{-1}. Thus, this mode is overlapped under the shoulder of above region.

From the vibrational analysis of a free water molecule, it has three types fundamental modes of vibrations. In this spectrum, these three types of vibrations are found and precisely assigned.

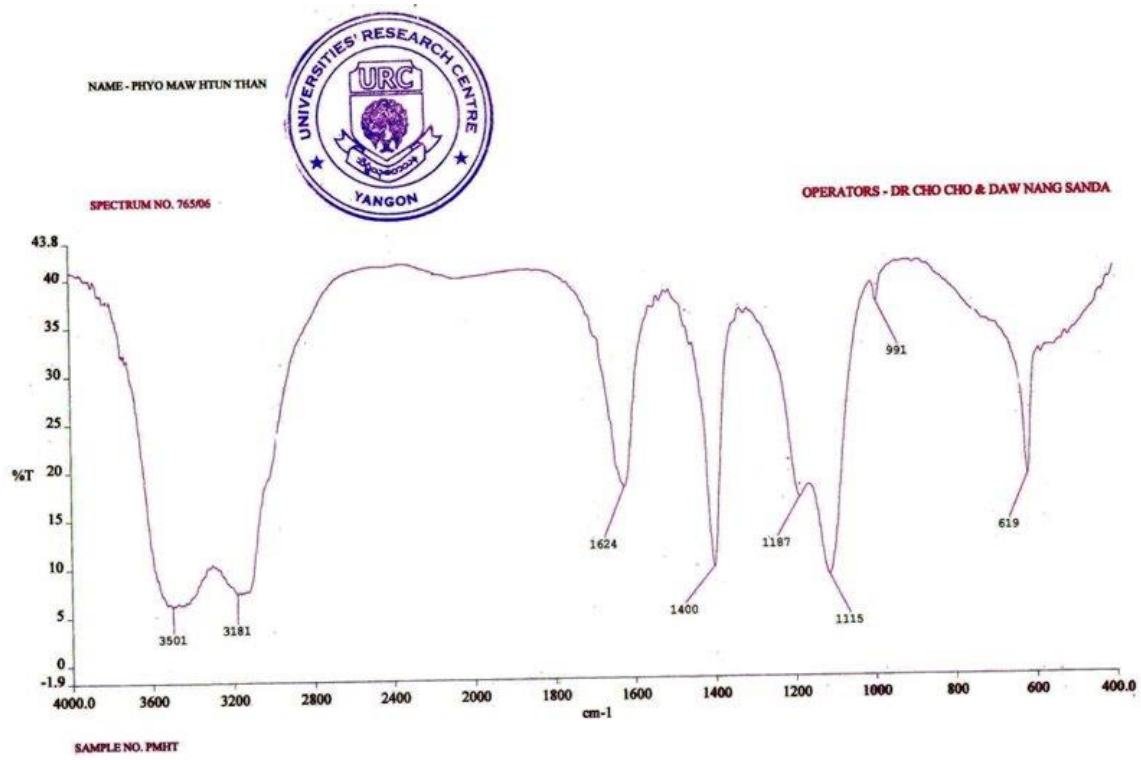

Fig 5.3 IR transmission spectrum of $ZnNH_4PO_4$ [ZAP] crystal with KBr disc method at room temperature

Table 5.3 Wavenumbers (Frequencies) and vibrational mode assignments of ZAP crystal

Sr No	Frequency (cm^{-1})	Mode Assignments	Types of Vibration
1	619	$\nu_4(PO_4^{3-})$	Asymmetric-Deformation
2	991	$\nu_1(PO_4^{3-})$	Symmetric-Stretching
3	1115/1187	$\nu_3(PO_4^{3-})$-doublet	Dipole
4	1400	$\nu_4(NH_4^{+})$	Asymmetric-deformation
5	1624	ν_2(H-O-H)	Asymmetric-stretching
6	3181	ν_3(H-O-H)	Symmetric-stretching
7	3501	ν_1(H-O-H)	Asymmetric-stretching

5.4 TG-DTA Study

Differential thermal analysis (DTA) is a thermal technique in which the temperature of a sample, compared with the temperature of a thermally inert material, is recorded as a function of the sample, inert material, or furnace temperature as the sample is heated or cooled at a uniform rate. Generally, phase transitions, dehydration, reduction, and some decomposition reactions produce endothermic effects, whereas crystallization, oxidation, and some decomposition reactions produce exothermic effects. At the same time, weight changes, which occur during some thermal changes, may also be measured. Hence, TG-DTA analysis, one able to determine whether the thermal changes are attributed to chemical changes such as absorption and decomposition or physical changes such as fusion.

Fig 5.4 shows the TG-DTA curves of $ZnNH_4PO_4$ [ZAP] crystal in the temperature range from 30°C to 550°C. First, two endothermic peaks in the DTA curve at 106°C and 135°C are indicated by the decomposition and dehydration or upon heating, ammonia, NH_3 and water, H-O-H molecules escape from the sample. These two peaks are overlapped in the temperature region started from 75°C to 175°C. Thus, these two processes are simultaneously occurred in the sample. While the weight loss of the sample was found on TGA curve about 69%. On further heating on the crystal, the constitutional water on the surface that produced during growth is evaporated at 300°C or pre-melting starts on the surface of the crystal. After reaching the temperature of 424°C, the sample was completely melted.

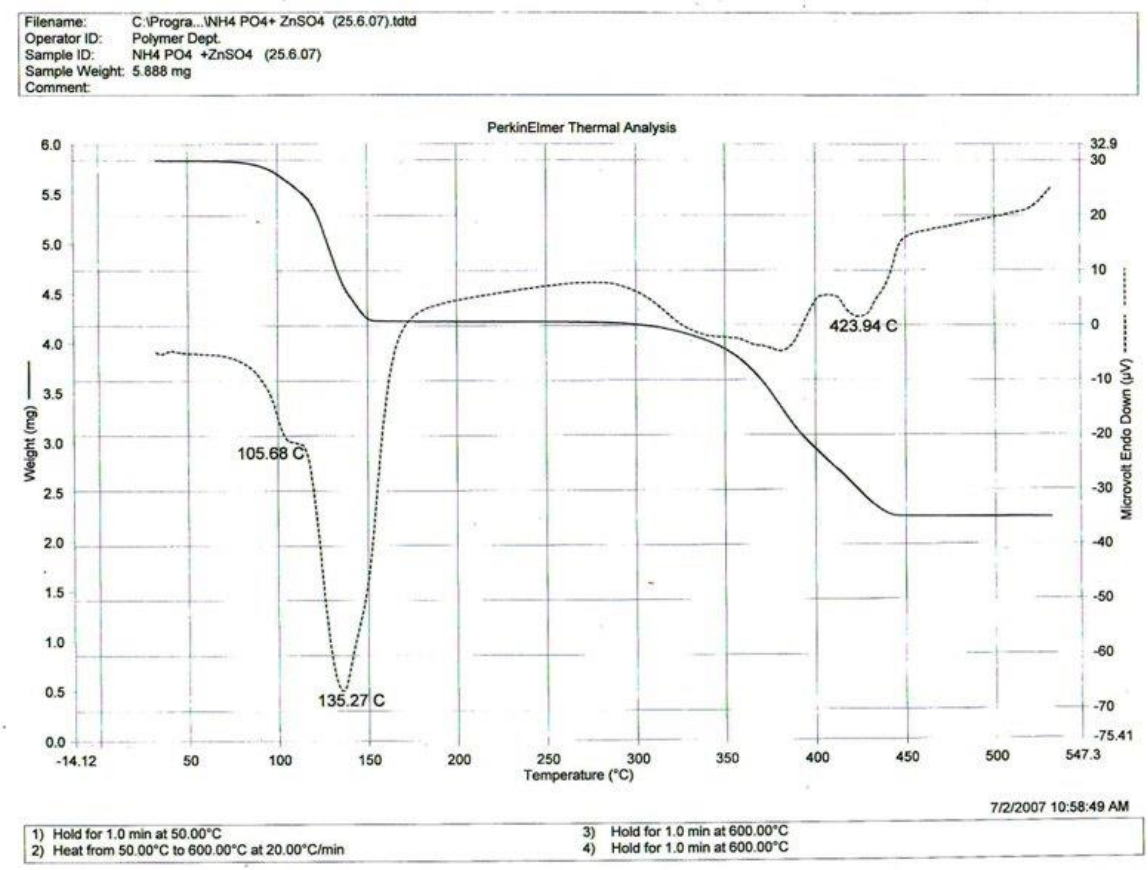

Fig 5.4 TGA-DTA curves of $ZnNH_4PO_4$ [ZAP] single crystal

5.5 Temperature Dependent Electrical Conductivity and Dielectric Study

According to theoretical approach, temperature–dependent electrical conductivity in ionic crystals can involve ionic migration and changes in the orientation of defects complexes. Ionic mobility is small charge, small size and lattice geometry. A highly charged ion will polarize, and be polarized by the ions of opposite charge as it moves past them, and this will increase the height of the energy barrier that inhibits a change of site.

Ionic conductivity of an ionic material obeys an Arrhenius formula $\sigma = \sigma_0 \exp(-E_i / kT)$, where σ is the conductivity, or ion drift in materials, σ_0 is the pre-exponential factor or slope of the conductivity curve, $E_i = E_j + \Delta H_s / 2$, E_i is the activation energy for ionic conduction, E_j is the barrier height, ΔH_s is thermal changes of Schottky defects accompanying the cation vacancy plus anion vacancy and ion vacancy plus interstitial ion, k is the Boltzmann constant and T is the absolute temperature. Arrhenius plot of the variation of dc electrical conductivity of the ZAP single crystal within temperature region of 30 °C (303 K) to 360 °C (633 K) is shown in Fig 5.5.

From the plot, it is found clearly that the conductivity of the sample is abruptly increased at the temperature 408 K because certain of the ionic bonds in the crystal must be broken before positive or negative ions of NH_3^+ and water molecules that contained from the crystal growth condition, are released (moved) to carry current. The agency that breaks the bond is usually thermal agitation.

Temperature dependent capacitances of $ZnNH_4PO_4$ [ZAP] crystal have been observed in the temperature range from 303 K to 633 K. The value of dielectric constant ε_r or ε have been calculated by the relation given below,

$$\varepsilon_r = \frac{1}{\varepsilon_0} \frac{Ct}{A}$$

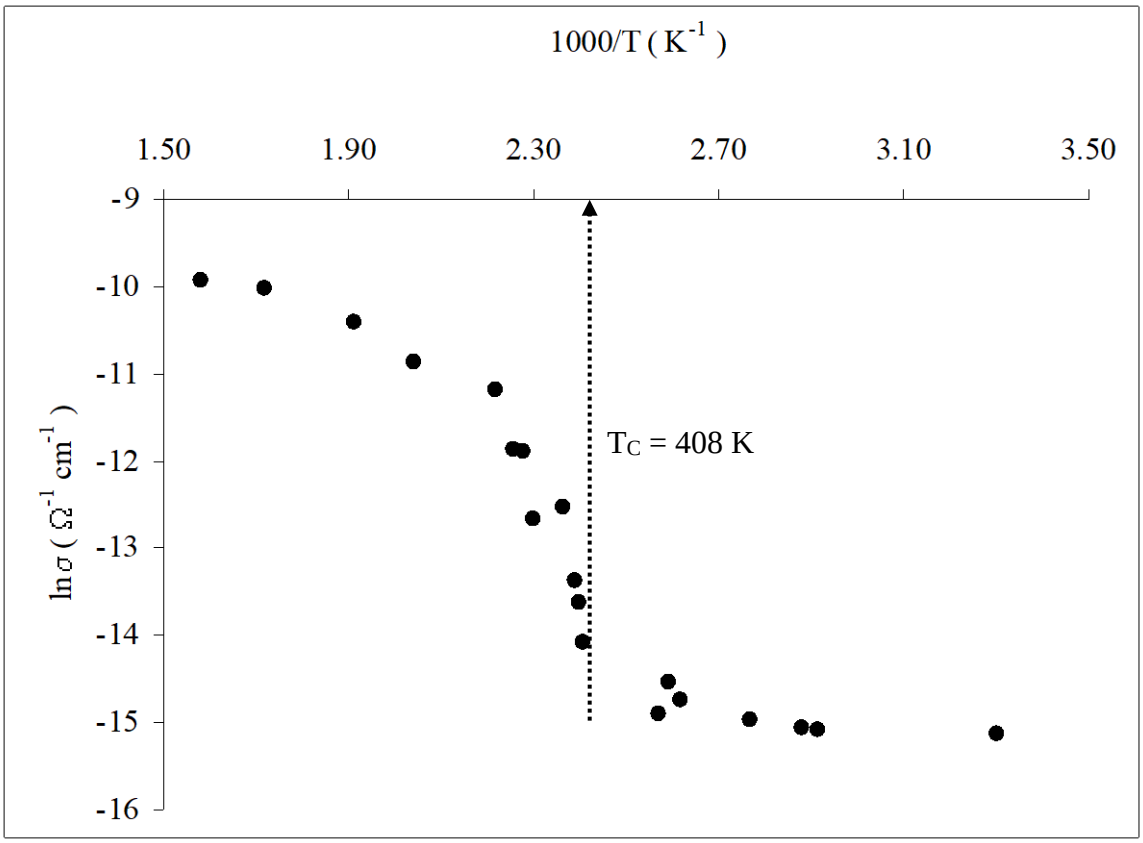

Fig 5.5 Variation of the dc electrical conductivity of $ZnNH_4PO_4$ [ZAP] single crystal at high temperature

where *C* is the capacitance, *t* is the thickness of the crystal, *A* is the cross-sectional (surface) area of the crystal and ε_0 is the permittivity of free space (8.854187817 x 10^{-12} Fm^{-1}). Temperature dependent dielectric constants of ZAP single crystal is shown in Fig 5.6. The value of the dielectric constants of the crystal was found in increased at 408K. Calculated values of electrical conductivity and dielectric constants of the crystal at room (RT) and at transition (T_C) temperatures are tabulated in Table 5.4. According to experimental results, this temperature (408K) can be taken as the decomposition temperature or phase transition (T_C) temperature of the crystal.

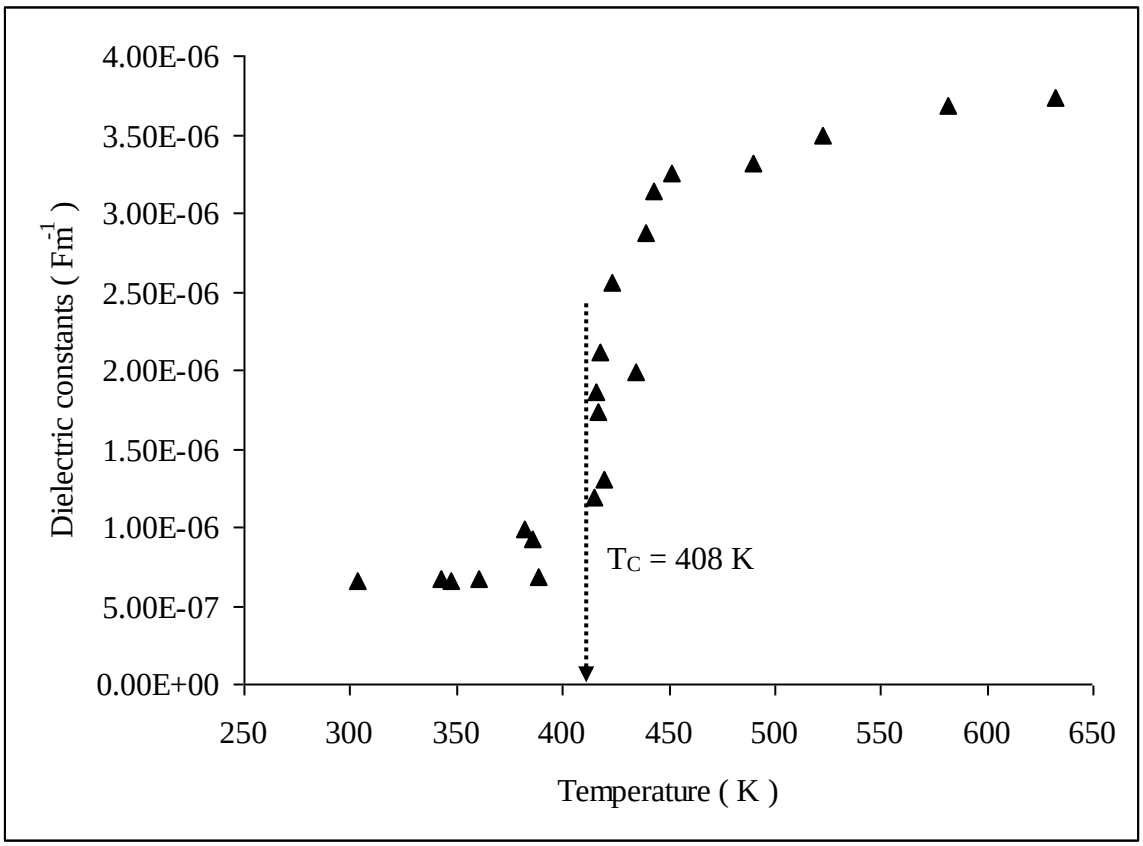

Fig 5.6 Temperature dependent dielectric constants of $ZnNH_4PO_4$ [ZAP] single crystal

Table 5.4 Calculated values of ionic conductivity, activation energy and dielectric constants of ZAP crystal at room and at high temperatures

Sr No	Temp (K)	σ ($\Omega^{-1}cm^{-1}$)	E_i (eV)	ε (Fm^{-1})
1	300 (RT)	2.69×10^{-7}	4.10×10^{-2}	6.62×10^{-7}
2	408 (T_C)	7.62×10^{-7}	5.14×10^{-2}	1.19×10^{-6}

5.6 Study on Light Dependent Electrical Characterizations

Light dependent electrical characterizations of $ZnNH_4PO_4$ [ZAP] single crystal were studied under the two different illuminations of light sources to investigate the light-sensitivity of the crystal. In the present work, the sample was directly used as the load (resistance) or light detector. When light of various intensities falling on the sample, the resistance and the voltage across the load were measured at the same time. This voltage is known to be photo-voltage. Also the light dependent capacitances of the sample were measured.

Characteristic curves of photocurrent against the light intensity (illumination) of the sample of two different light sources are shown in Fig 5.7(a) and Fig 5.7(b) respectively. According to experimental results, the output photocurrents of the crystal were found to be linearly increased by the increasing of light intensity (illumination) under the investigation of two different light sources of without electric field. The photosensitivity of the crystal can be regarded as the pre-exponential factor or slope of the photocurrent against the light intensity curve or photocurrent per unit area under the illumination because the crystal was used as the directly light detector in this work. The obtained light-sensitivities of the ZAP single crystal under different illuminations are tabulated in Table 5.5.

Characteristic curves of dielectric constant against the light intensity (illumination) of the sample of two different light sources are shown in Fig 5.8(a) and Fig 5.8(b) respectively. As shown in these figures, the dielectric constant of the sample under two different illuminations are found in linearly increased with increasing illuminations of light.

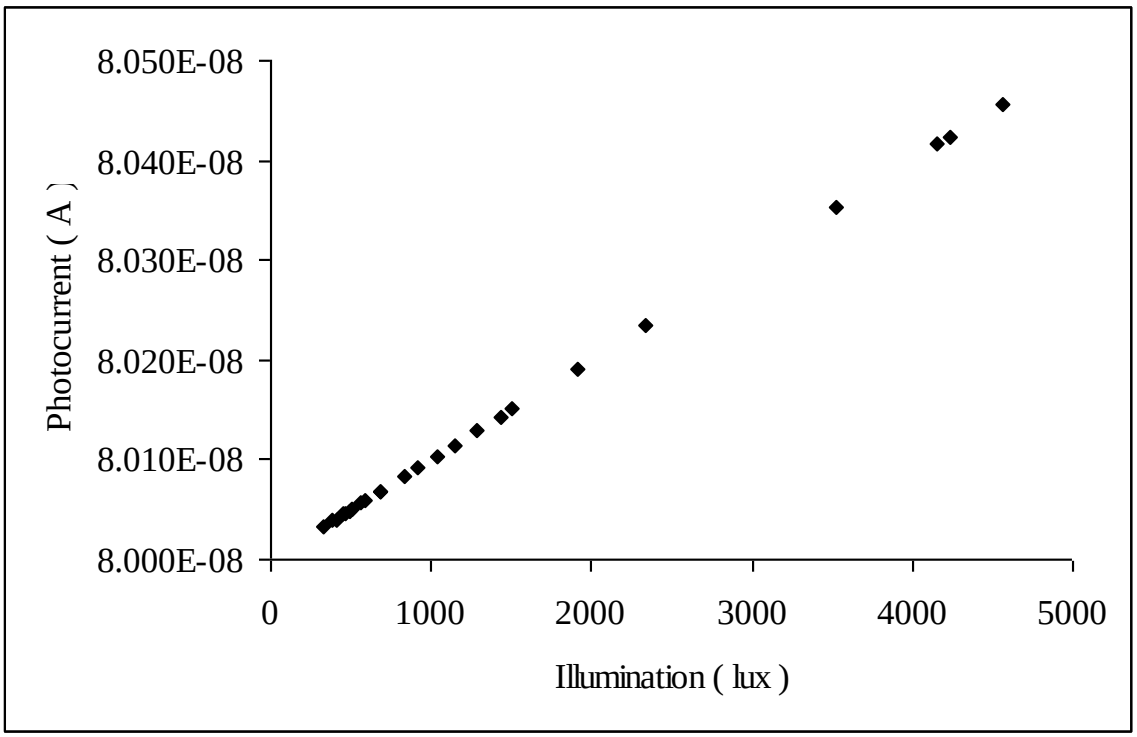

Fig 5.7(a) Characteristic curve of photocurrent against the illumination of ZAP crystal under 20W light source

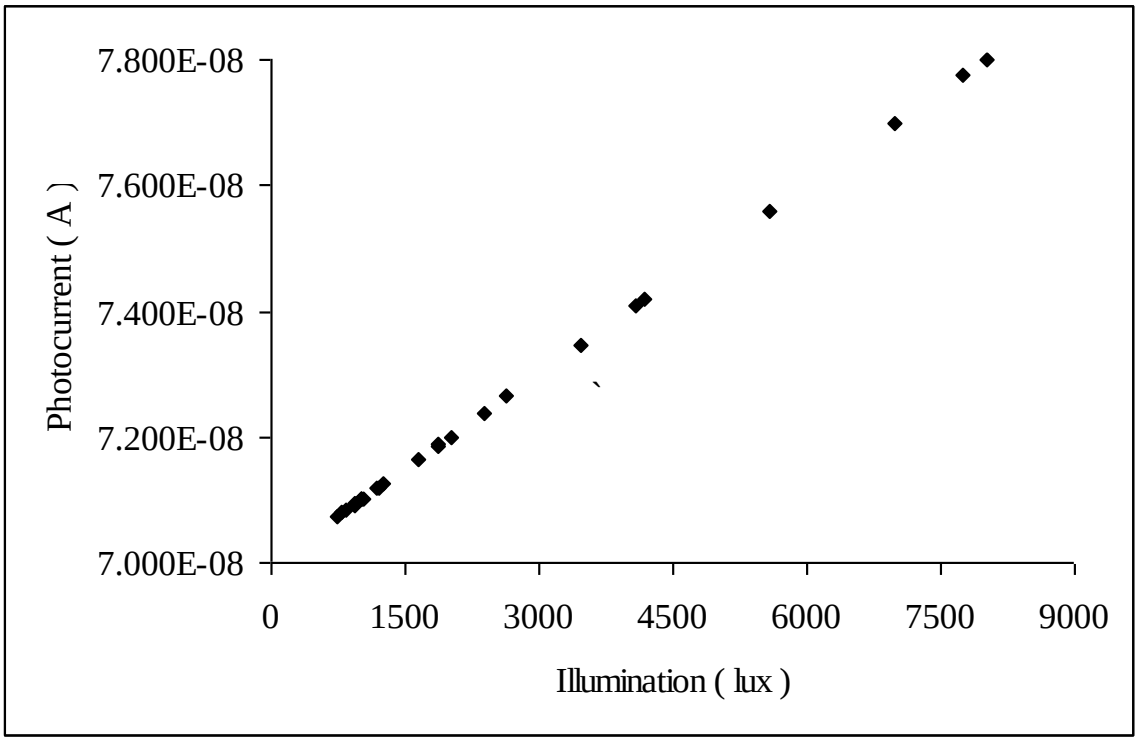

Fig 5.7(b) Characteristic curve of photocurrent against the illumination of ZAP crystal under 100W light source

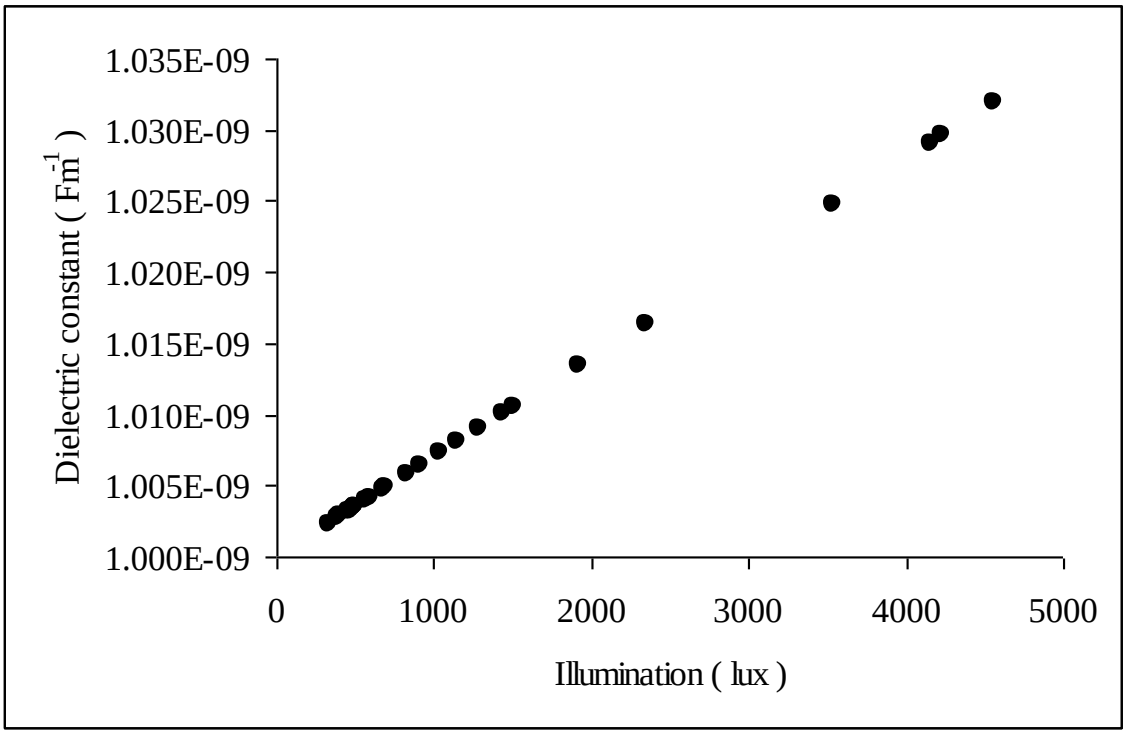

Fig 5.8(a) Characteristic curve of dielectric constant against the illumination of ZAP crystal under 20W light source

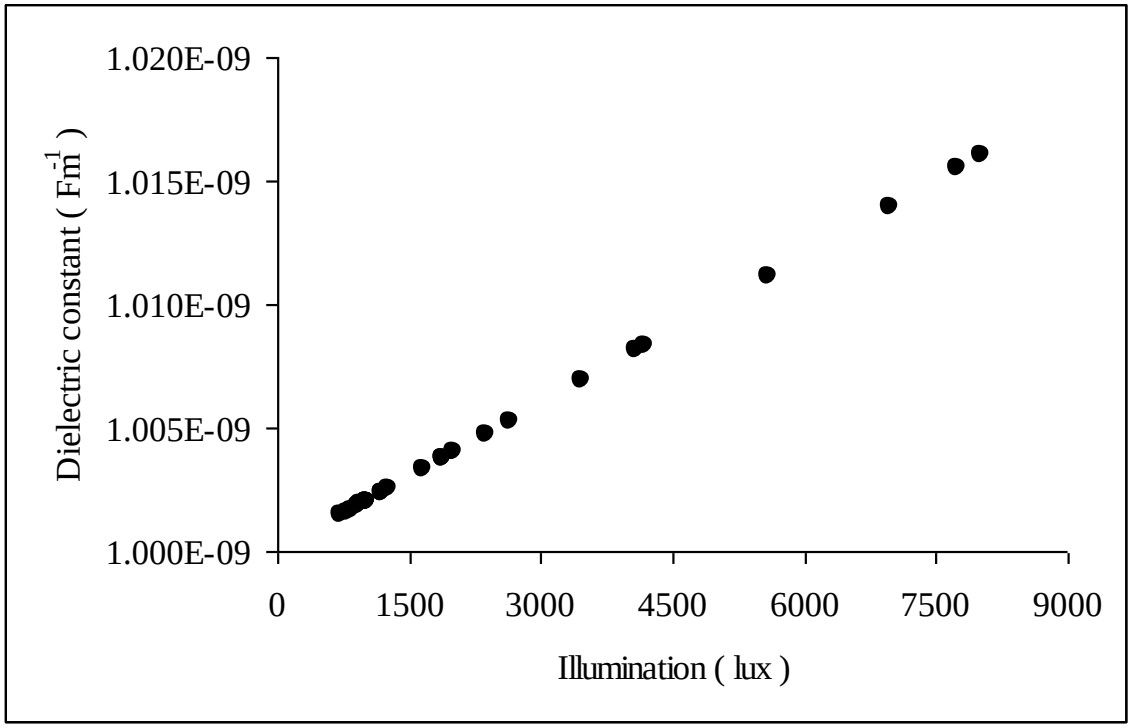

Fig 5.8(b) Characteristic curve of dielectric constant against illumination of ZAP crystal under 100W light source

Table 5.5 Photo-sensitivities of ZAP single crystal under two different illuminations of light sources

Sr No	Light source (W)	Photosensitivity (A/lux cm^2)
1	20	1.00×10^{-13}
2	100	1.00×10^{-12}

5.7 Conclusion

Characterizations of $ZnNH_4PO_4$ [ZAP] single crystal were studied in this work. According to XRD analysis, ZAP crystal belongs to orthorhombic structure and its lattice constants are obtained as a = 6.00 Å, b = 12.57 Å and c = 16.12 Å respectively. Four fundamental modes of phosphate are found in Raman spectrum. In this spectrum, the line at 1622 cm^{-1} is a bending vibration of the ammonium and the line at 3092 cm^{-1} is a symmetric-stretching vibration of water. From the FTIR spectrum, three fundamental modes of phosphate, one mode of ammonium and three modes of water molecules are observed and assigned.

TGA-DTA curves of $ZnNH_4PO_4$ [ZAP] single crystal show that two endothermic peak on DTA curve at 106 °C and 135 °C are indicated by the decomposition and dehydration or upon heating, ammonia, NH_3 and water, H-O-H molecules escape from the sample. These two processes are simultaneously occurred in the sample while the weight loss of 69% on TGA curves simultaneously. Temperature dependent electric conductivity of the crystal was increased with increasing temperature and the conductivity was abruptly increased at 135°C. This temperature is agreed with the TG-DTA results. According to photoconductivity results, ZAP crystal is more sensitive to 100W light source than 20W light source.

REFERENCES

1. Agui A and Tominaga Y 1993 J Phys Soc Jpn 62, (2), 87
2. Arivuoli D 2001 PRAMANA_J Phys 57, (5&6), 871
3. Aung Myat Kyaw et al 2005 JMAAS 3, (3), 43
4. Banwell C N and McCash E M 1994 "Fundamentals of Molecular Spectroscopy" (London: McGraw–Hill)
5. Barrow G M 1962 "Introduction to Molecular Spectroscopy" (Tokyo: McGraw-Hill)
6. Clegg W 2003 "Crystal Structure Determination" (Oxford:Oxford Science)
7. Dann S E 2000 "Reaction and Characterization of Solids" (Cambridge: RSC)
8. Freeda T H and Mahadevan C 2001 PRAMANA-J Phys 57, (4), 829
9. Grasselli J G and Bulkin B J 1991 "Analytical Raman Spectroscopy" (New York: Wiley)
10. Hendra P, Jones C and Warnes G 1991 "Fourier Transform Raman Spectroscopy" (Singapore: Ellis Horwood)
11. http://gabby.osha-slc.gov/OshStd_data/1910.1048_App_A.html
12. Irene E A 2005 "Electronic Materials Science" (New York: Wiley)
13. Kittle C 1999 "Introduction to Solid State Physics" (Singapore: Wiley)
14. Long D A 1988 "Raman Spectroscopy" (New York: Wiley)
15. Puri R K and Babbar V K 2003 "Solid State Physics and Electronics" (New Delhi: S CHAND)
16. Raghavan V 2003 "Materials Science and Engineering" (New Delhi: Prentice Hall)
17. Ross S D 1972 "Inorganic Infrared and Raman Spectra" (London: McGraw-Hill)
18. Tanaka H and Tatsuzaki I 1984 Solid State Comm 49, (2), 153
19. Theivanayagom M & Mahadevan C 2001 Bull Master Sci 24, (5), 441
20. Win Kyaw et al 2004 JARC-YU, 1, (1), 132
21. Xu Y 1991 "Ferroelectric Materials and Their Applications" (North-Holland: Elsevier)